uOttawa

L'Université canadienne
Canada's university

FACULTÉ DES ÉTUDES SUPÉRIEURES ET POSTOCTORALES

uOttawa

L'Université canadienne
Canada's university

FACULTY OF GRADUATE AND POSDOCTORAL STUDIES

Yu Zhang

AUTEUR DE LA THÈSE / AUTHOR OF THESIS

M. A. Sc. Mechanical Engineering

GRADE / DEGREE

Department of Mechanical Engineering

FACULTÉ, ÉCOLE, DÉPARTEMENT / FACULTY, SCHOOL, DEPARTMENT

Finite Element Simulation of Innovative Manufacturing Processes for Tube Fittings

TITRE DE LA THÈSE / TITLE OF THESIS

Dr. David Redekop

DIRECTEUR (DIRECTRICE) DE LA THÈSE / THESIS SUPERVISOR

CO-DIRECTEUR (CO-DIRECTRICE) DE LA THÈSE / THESIS CO-SUPERVISOR

EXAMINATEURS (EXAMINATRICES) DE LA THÈSE / THESIS EXAMINERS

Dr. C-L. Tan

Dr. G. Rouhi

Gary W. Slater

Le Doyen de la Faculté des études supérieures et postdoctorales / Dean of the Faculty of Graduate and Postdoctoral Studies

Finite Element Simulation of Innovative Manufacturing Processes for Tube Fittings

by

Yu Zhang

A thesis submitted to the Faculty of Graduate and Postdoctoral Studies in partial fulfilment of the requirements for the degree of

Master of Applied Science

in Mechanical Engineering

Ottawa-Carleton Institute for Mechanical and Aerospace Engineering

University of Ottawa

Ottawa, Canada

Your file Votre référence
ISBN: 978-0-494-41689-1
Our file Notre référence
ISBN: 978-0-494-41689-1

Acknowledgements

I would like to express my sincere gratitude to my supervisor, Dr. David Redekop, for his patient guidance, continuous encouragement and valuable suggestions throughout the research.

I express my deep gratefulness to my parents for their everlasting love, support, and encouragement.

I wish to express my appreciation to the academic members and the staff of the Department of Mechanical Engineering.

Abstract

Tube fittings are widely used in the pressure vessel industry. Current research on tube fittings serves to determine means of decreasing the cost and increasing the efficiency of their manufacture. With this motivation, several new tube forming processes have been proposed in recent years. The current study focuses on the finite element simulation of two new manufacturing processes for tube fittings; i.e. hydroforming and tube push-bending.

For tube hydroforming, used to produce T and Y joints, there is a working range defined by the combination of internal pressure and axial load. To ensure that a satisfactory product is obtained, it is essential that the loading path be inside the working range. The working range for several tube hydroforming models are predicted, and the results are validated with existing theoretical and experimental values.

The new tube push bending process has the advantage that tube bends with a small bending radius can be produced. In this study, finite element simulations are carried out to demonstrate this advantage. The spring-back and material waste factors are determined through simulation, as well as the maximum axial load. The results obtained are validated against existing theoretical and experimental values.

The study ends with some conclusions about the suitability of finite element simulations in tube forming processes, and with some suggestions for further research.

Contents

List of Tables

List of Figures

Chapter 1
Introduction

1.1 Tube fittings

Tube fittings are used in pipe and plumbing systems to connect straight pipe or tubing sections, to adapt to different sizes or shapes, and to regulate fluid flow. Bent, T and Y tube fittings are the most common tube-to-tube fittings. T and Y shaped tube fittings (or T and Y joints) are used to connect three pipes. Compared with T joints, Y joints have an advantage of flexible installation, but are more difficult to make. The conventional way to make T and Y joints is forging. Bent tubes (elbows) are used to change the direction of a pipe by connecting two pipes with a specific angle. They do this with the aid of pipe fittings. The ends may be machined for butt welding, threaded (usually female), or socketed, etc. Most elbows are available in either short radius or long radius form. Short radius elbows are universally available; long radius elbows are readily available in sewage, central vacuums, and copper for houses with copper drains.

1.2 Tube hydroforming (THF)

In recent years, some new and effective manufacturing techniques have been invented. An important technique is called "hydroforming", which uses high pressure hydraulic pressure to make tubes bulge and under the effect of a die, to make desired tube shapes. Figure 1.1 illustrates the THF process for a T-joint. External axial loads F are applied on

the punches, and the tube blank is subjected to high pressure liquid. The die defines the desired shape of the product. Under the combined effect of the axial loads and internal pressure, the tube starts to bulge into the cavity of the die and the length of the tube length becomes shorter than its original length. At last, when the tube fully fills the die, a joint is made.

Figure 1.2 shows the principle of Y-hydroforming. It is very similar to T-hydroforming. The main difference is that the angle between the axes of the protrusion part and the original tube axis is not 90 degrees in Y-hydroforming.

THF has several advantages compared with conventional industrial processes. It reduces the processing time and material cost. As a welding process is not required, a hydroformed part has good consistency. THF parts are commonly used in the automotive industry. Many THF products are used in a car body, such as roof header, instrument panels, radiator frame, engine cradle, and roof rails. Many additional parts are being considered for THF technique, and more automotive parts will be made using this method in the future.

During the last five years or so, the THF method has attained major importance in the fabrication of T-joints and Y-joints. A closed seamless T tube is obtained which is low cost and meets of traditional requirements. The process can have unsatisfactory results such as bursting, wrinkling and incomplete forming if the axial feeding rate, internal pressure, and other factors are not properly controlled. So, it is very important to find an optimal

loading path for different cases.

1.3 Tube push-bending

The use of modern methods to fabricate curved tubes (elbows) has become crucial for success in the pipe forming industry. There is a need to decrease component costs and to improve component properties. The costs can be decreased by increasing production rates and reliability, while properties can be improved by offering improved process characteristics. These requirements lead to the need to develop new, innovative manufacturing techniques, which can provide a significant advantage over competing processes. Under such industrial background a new method of cold forming, referred to as push-bending, was proposed recently. The most obvious characteristic of push-bending is the use of a mandrel inside the entire tube part to prevent buckling of the tube's wall.

Figures 1.3 and 1.4 give an illustration of the tube push-bending. The forming apparatus, consisting of the main components of tube, mandrel, die, and plunger (punch) are shown in figure 1.3. The tube's position after forming and the use of the internal pressure approximation for the elastomer rod action are shown in figure 1.4. The tube itself is placed inside a die and a punch located at the end of the tube exerts an axial load on the tube and rod. This results in the tube and rod being pushed into a curved part of the die, and the generation of an internal pressure in the tube. This pressure inhibits wrinkling, and thus leads to a product with improved characteristics.

1.4 Nonlinear plastic analysis

The forming processes are non-linear problems and involve plasticity. It is necessary to introduce the basic principles of non-linear plastic analysis.

The finite element equilibrium equation derived for linear elastic static analysis (Bathe, 1996) is:

$$KU = R \tag{1.1}$$

where K is the linear stiffness matrix, R is the load matrix, U is the displacement matrix.

In metal forming problems, nonlinearity arises in three contexts, which are large displacement, large strain, and materially nonlinearity. The component boundary contact problem is also nonlinear. In LS-DYNA, Lagrangian algorithm was employed to deal with large displacement and large strain problems (Eulerian algorithm is good for fluid mechanics).

The basic problem in general nonlinear static analysis is to find the state of equilibrium of a body corresponding to the applied loads (Bathe, 1996), which is shown as:

$${}^{t}R - {}^{t}F = 0 \tag{1.2}$$

where the vector ${}^{t}R$ lists the external nodal point forces at time t and the vector ${}^{t}F$ lists the nodal point forces that correspond to the element stresses at time t. Because it is assumed that at any time the relation must be satisfied, in an incremental step-by-step

solution, we have at time $t+\Delta t$:

$$^{t+\Delta t}R - {}^{t+\Delta t}F = 0 \tag{1.3}$$

Since the solution is known at time t, we have

$$^{t+\Delta t}F = {}^{t}F + F \tag{1.4}$$

where F is the increment in nodal point forces corresponding to the increment in element displacements and stresses from time t to time $t+\Delta t$. The vector F can be approximately expressed as:

$$F \doteq {}^{t}KU \tag{1.5}$$

where $\doteq$ is the approximate equal sign, U is a vector of incremental nodal point displacements and

$$^{t}K = \frac{\partial {}^{t}F}{\partial {}^{t}U} \tag{1.6}$$

Substituting (1.5) and (1.4) into (1.3), we obtain

$$^{t}KU = {}^{t+\Delta t}R - {}^{t}F \tag{1.7}$$

and solving for U, we can approximately calculate the displacements at time $t+\Delta t$, as:

$$^{t+\Delta t}U \doteq {}^{t}U + U \tag{1.8}$$

For materially-nonlinear analysis, a proper material model should be defined. In this thesis power law plasticity was employed. In power law plasticity with isotropic hardening, the yield stress (LS-DYNA Theory Manual, 2006) is defined by (see figure

1.5):

$$\sigma_y = k\varepsilon^n = k(\varepsilon_{ye} + \bar{\varepsilon}^p)^n \tag{1.9}$$

where, σ_y is the yield stress, k is the strength coefficient, ε_{ye} is the elastic strain to yield, $\bar{\varepsilon}^p$ is the effective plastic strain, n is the hardening parameter.

If σ_y is unknown for the material, the strain to yield can be still evaluated by LSDYNA. For such case, σ_y should be set to zero in LS-DYNA (or leave it blank), the strain to yield ε_{yp} can be found by solving the intersection of the linearly elastic loading equation with the strain hardening equation:

$$\sigma = E\varepsilon \tag{1.10}$$

$$\sigma = k\varepsilon^n \tag{1.11}$$

which gives the elastic strain at yield as:

$$\varepsilon_{ye} = \left(\frac{E}{k}\right)^{\left[\frac{1}{n-1}\right]} \tag{1.12}$$

If the yield stress σ_y is set to non-zero then:

$$\varepsilon_{ye} = \left(\frac{\sigma_y}{k}\right)^{\left[\frac{1}{n}\right]} \tag{1.13}$$

The von Mises stress is usually used in finite element analysis. It is an important quantity for plasticity analysis. It is also used in ductile fracture criterion (section 3.3). It is defined (Hill, 1950) as:

$$\sigma_y = \sqrt{\frac{(\sigma_1 - \sigma_2)^2 + (\sigma_2 - \sigma_3)^2 + (\sigma_1 - \sigma_3)^2}{2}} \tag{1.14}$$

where σ_1, σ_2, σ_3 are the principal stresses. Usually, the principal stresses are not given by the post-processor. Instead, the stress tensor σ_{ij} in the defined coordinate is given. In order to evaluate the principal stresses, some mathematical calculations need to be done.

Assume a 3D stress tensor σ_{ij} is given, which has a matrix form as $\begin{bmatrix} \sigma_{11} & \sigma_{12} & \sigma_{13} \\ \sigma_{21} & \sigma_{22} & \sigma_{23} \\ \sigma_{31} & \sigma_{32} & \sigma_{33} \end{bmatrix}$. This matrix is symmetric, i.e. $\sigma_{12} = \sigma_{21}$, $\sigma_{13} = \sigma_{31}$, and $\sigma_{23} = \sigma_{32}$. The principal stresses can be found by solving the following equation:

$$\left|\sigma_{ij} - \lambda\delta_{ij}\right| = \lambda^3 - I_1\lambda^2 + I_2\lambda - I_3 = 0 \tag{1.15}$$

Three real roots (not imaginary due to the symmetry of the stress tensor) $\lambda_1 = \sigma_1$, $\lambda_2 = \sigma_2$, and $\lambda_3 = \sigma_3$ are the principal stresses. I_1, I_2 and I_3 are the first, second, and third deviatoric stress invariants, respectively. Their values do not change regardless of the orientation of the coordinate system. They are defined by the following equations:

$$I_1 = \sigma_{11} + \sigma_{22} + \sigma_{33} \tag{1.16}$$

$$I_2 = \sigma_{11}\sigma_{22} + \sigma_{22}\sigma_{33} + \sigma_{11}\sigma_{33} - \sigma_{12}^2 - \sigma_{23}^2 - \sigma_{13}^2 \tag{1.17}$$

$$I_3 = \sigma_{11}\sigma_{22}\sigma_{33} + 2\sigma_{12}\sigma_{23}\sigma_{31} - \sigma_{12}^2\sigma_{33} - \sigma_{23}^2\sigma_{11} - \sigma_{13}^2\sigma_{22} \tag{1.18}$$

The hydrostatic stress (mean stress, σ_h, σ_m) is an important parameter in FEM simulation, and is also used in ductile fracture analysis (section 3.3). It can be found by the following equation:

$$\sigma_h = \sigma_m = \frac{1}{3}(\sigma_{11} + \sigma_{22} + \sigma_{33}) = \frac{1}{3} I_1 \tag{1.19}$$

1.5 Finite element analysis

The finite element method (FEM) was first suggested by Courant in 1943, and has been developing rapidly since the 1960s with the wide use of digital computers. The finite element method was initially developed on a physical basis for the analysis of problems in structural mechanics. However, it was soon used in many other classes of problems such as electronics and quantum mechanics.

The finite element method is an important approach in engineering analysis. Due to the complexity of many practical engineering problems, design and analysis are difficult to carry out by conventional analytical means. One of the steps in finite element analysis is choosing an appropriate mathematical model. Then, proper finite element procedures should be employed to solve the chosen model. By judging the results from finite element simulations, the mathematical model can be improved until the results of simulation agree with the practice within an acceptable error.

By now many FEM software packages have been developed. With the aid of the strong calculation abilities of computers, solving an engineering problem has become accurate and fast. Generally, there are three phases in a computer-aided engineering task solved by FEM; they are pre-processing, solution, and post-processing.

In the pre-processing phase, finite element models are created with initial definitions of geometry, mesh, material properties, loading and boundary conditions. In the solution

phase, the computer solves the mathematical model by using the finite element procedure, and the finite element solution is obtained. To interpret the results from the finite element solution, visualization tools are used and this is referred to as "post-processing". In order to obtain an effective and reliable model, the model should be refined or redesigned, then re-solved by repeating the above steps.

Many companies and researchers deal with engineering problems by finite element simulation. The advantages of FEM are obvious. It dramatically reduces the experimentation costs, and it is very easy to change the model's design. Furthermore, the visualized post-processed results are very friendly to users.

Since tube forming processes are nonlinear dynamic problems, the damping and inertia effects must be considered. In this research, the viscoelasticity/viscoplasticity is not a consideration, so the visco-damping effect is ignored. In FEM analysis, the governing equation for dynamic response (Bathe, 1996) can be written as:

$$M\ddot{U}+C\dot{U}+KU=R \tag{1.20}$$

where M, C, and K are the mass, damping, and stiffness matrices; R is the vector of externally applied loads; U, $\dot{U}$, and $\ddot{U}$ are the displacement, velocity, and acceleration vectors. The numerical integration methods in the time domain should be considered. The time domain is divided into discrete time intervals Δt. This means that, the equation (1.20), which includes the effect of inertia and damping forces is sought at discrete time points within the interval of solution (Bathe, 1996). Therefore, all solution

techniques employed in static analysis can also be used in dynamic analysis.

Distinguished by the integration approaches, there are implicit and explicit solutions. The characteristics of explicit solutions are (Wu, 2003 and Bath, 1996): accurate for dynamic and highly-nonlinear problems, possess a simple logic, the time should be kept smaller than a crucial value, and they do not have the iteration convergence issue. The characteristics of implicit solutions are: they are accurate for static and medium nonlinear problems, possess a complex logic, time step should be equal to the stability limit.

In the tube forming area, several software packages are commonly used. They are DEFORM2D, DEFORM3D (implicit software packages), PAM-STAM and LS-DYNA (explicit software packages). In this thesis, all tube forming processes are highly nonlinear problems, and to make sure of the accuracy of the results, the time step should be kept small. Under this consideration, an explicit software package is the better choice.

Based on these considerations, LS-DYNA was used to solve the finite element problems in this thesis. It is a general-purpose explicit FEM package that has the capability to determine the highly nonlinear dynamic response of three-dimensional inelastic structures. The pre-processor was FEMB (Finite Element Model Builder), which has a wide application in computer-aided engineering. The post-processor was Post GL, which has been designed to work more integrally with LS-DYNA and has high-end graphics capabilities. This package was also preferred in the recent thesis by Yao (2005), which dealt with the bulge forming of a toroidal shell.

1.6 Shell applications in finite element analysis

One of the essential decisions to be made is which type of element to use for the finite element simulation. The type of element tells the solver "in which way to solve a meshed model". There are three basic element types in LS-DYNA, which are respectively beam element, shell/plate element, and solid element. A shell element is characterized by one dimension being smaller than the other two dimensions; use of three-dimensional elements like solid elements would involve many unused degrees of freedom. To simulate manufacturing tube fittings, the shell element is selected. The reasons for the use of the shell element are: the solid element is too general for such specific problems, and the beam element can not describe the cross-sectional deformations of a tube.

In finite element analysis, a shell element is a 3D element for which one of the dimensions is small with respect to the other two. Shell elements are described by shell theories, for which extensive documentation is available in the literature (Baker *et al*, 1972 and Soedel, 1981).

1.7 Belytschko-Lin-Tsay shell element

In 1981, Belytschko and Tsay presented a shell model which was implemented in LS-DYNA as a computationally efficient shell element. It has five through-thickness integration points and requires 725 mathematical operations compared to 4066 operations for the alternative Hughes-Liu shell element (*LS-DYNA Theory Manual*, 2006). In this

thesis, the meshes of the models are refined, which requires a long processing time, so, the computational efficiency is quite important.

As the shell element is used in all finite element models of this thesis, the principles of the theory will be presented in detail.

This element is a quadrilateral shell element. The mid-surface of this element is defined by the location of the element's four corner nodes, and the deformation in the shell coordinate system is defined in terms of these nodal coordinates. The construction of the co-rotational coordinate system begins by calculating a unit vector normal $\hat{e}_3$ to the main diagonals of the element (*LS-DYNA Theory Manual*, 2006).

$$\hat{e}_3 = \frac{s_3}{\|s_3\|} \tag{1.21}$$

$$\|s_3\| = \sqrt{s_{31}^2 + s_{32}^2 + s_{33}^2} \tag{1.22}$$

$$s_3 = r_{31} \times r_{42} \tag{1.23}$$

where the subscript (^) indicate the local (element) coordinate, the vectors s_3, r_{31}, r_{42} and $\hat{e}_3$ are defined in figure 1.6.

To make it convenient for interpreting the element stresses, which are defined in the local $\hat{x}-\hat{y}$ coordinate system, it is desired to establish the local x-axis, $\hat{x}$, approximately along the element edge between nodes 1 and 2. Vectors s_1 and $\hat{e}_1$, which are nearly parallel to the vector r_{21}, are introduced (*LS-DYNA Theory Manual,*2006):

$$s_1 = r_{21} - (r_{21} \cdot \hat{e}_3)\hat{e}_3 \tag{1.24}$$

$$\hat{e}_1 = \frac{s_1}{\|s_1\|} \tag{1.25}$$

The remaining unit vector $\hat{e}_2$ can be obtained from the cross product:

$$\hat{e}_2 = \hat{e}_3 \times \hat{e}_1 \tag{1.26}$$

The global components of this co-rotational triad define a transformation matrix between the global and local element coordinate systems. This transformation operates on vectors with global components $A = (A_x, A_y, A_z)$ and element coordinate components $\hat{A} = (\hat{A}_x, \hat{A}_y, \hat{A}_z)$, and is defined as (*LS-DYNA Theory Manual,* 2006):

$$\{A\} = \begin{Bmatrix} A_x \\ A_y \\ A_z \end{Bmatrix} = \begin{bmatrix} e_{1x} & e_{2x} & e_{3x} \\ e_{1y} & e_{2y} & e_{3y} \\ e_{1z} & e_{2z} & e_{3z} \end{bmatrix} \begin{Bmatrix} \hat{A}_x \\ \hat{A}_y \\ \hat{A}_z \end{Bmatrix} = [\mu]\{\hat{A}\} \tag{1.27}$$

where e_{ix}, e_{iy}, e_{iz} are the global components of the element coordinate unit vectors, and $[\mu]$ is a matrix that is composed of e_{ix}, e_{iy}, and e_{iz}. The inverse transformation is defined as:

$$\{\hat{A}\} = [\mu]^{-1}\{A\} \tag{1.28}$$

The displacement of any point in the shell is partitioned into a mid-surface displacement (nodal translations) and a displacement associated with rotations of the element's fibers (nodal rotations). The Belytschko-Lin-Tsay shell element uses the Mindlin (1951) theory of plates and shells to partition the velocity of any point in the

shell as:

$$v = v^m - \hat{z}e_3 \times \dot{\theta} \tag{1.29}$$

where v^m is the velocity of the mid-surface, $\dot{\theta}$ is the angular velocity vector, and $\hat{z}$ is the distance along the fiber direction (thickness) of the shell element. The corresponding co-rotational components of the velocity strain are given by (*LS-DYNA Theory Manual,* 2006):

$$\hat{d}_{ij} = \frac{1}{2}\left(\frac{\partial \hat{v}_i}{\partial \hat{x}_j} + \frac{\partial \hat{v}_j}{\partial \hat{x}_i}\right) \tag{1.30}$$

Substitute equation (1.29) into (1.30), we have the following velocity-strain relations:

$$\hat{d}_x = \frac{\partial \hat{v}_x^m}{\partial \hat{x}} + \hat{z}\frac{\partial \hat{\theta}_y}{\partial \hat{x}} \tag{1.31}$$

$$\hat{d}_y = \frac{\partial \hat{v}_y^m}{\partial \hat{y}} - \hat{z}\frac{\partial \hat{\theta}_x}{\partial \hat{y}} \tag{1.32}$$

$$2\hat{d}_{xy} = \frac{\partial \hat{v}_x^m}{\partial \hat{y}} + \frac{\partial \hat{v}_y^m}{\partial \hat{x}} + \hat{z}\left(\frac{\partial \hat{\theta}_y}{\partial \hat{y}} - \frac{\partial \hat{\theta}_x}{\partial \hat{x}}\right) \tag{1.33}$$

$$2\hat{d}_{yz} = \frac{\partial \hat{v}_z^m}{\partial \hat{y}} - \hat{\theta}_x \tag{1.34}$$

$$2\hat{d}_{yz} = \frac{\partial \hat{v}_z^m}{\partial \hat{x}} + \hat{\theta}_y \tag{1.35}$$

The above velocity-strain relations need to be evaluated within the shell. Standard bilinear nodal interpolation is employed. These interpolations relations are given by (*LS-DYNA Theory Manual,* 2006):

$$v^m = N_I(\xi,\eta)v_I \tag{1.36}$$

$$\theta^m = N_I(\xi,\eta)\theta_I \tag{1.37}$$

$$x^m = N_I(\xi,\eta)x_I \tag{1.38}$$

where the subscript I is summed over all the nodes of the element and the nodal velocities are obtained by differentiating the nodal coordinates with respect to time. The bilinear shape functions are (*LS-DYNA Theory Manual,* 2006):

$$N_1 = \frac{1}{4}(1-\xi)(1-\eta) \tag{1.39}$$

$$N_2 = \frac{1}{4}(1+\xi)(1-\eta) \tag{1.40}$$

$$N_3 = \frac{1}{4}(1+\xi)(1+\eta) \tag{1.41}$$

$$N_4 = \frac{1}{4}(1-\xi)(1+\eta) \tag{1.42}$$

When $\xi = 0$ and $\eta = 0$, the velocity-strain values are for the point located at center of the element. This yields:

$$\hat{d}_x = B_{1I}\hat{v}_{xI} + \hat{z}B_{1I}\hat{\theta}_{yI} \tag{1.43}$$

$$\hat{d}_y = B_{2I}\hat{v}_{yI} - \hat{z}B_{2I}\hat{\theta}_{xI} \tag{1.44}$$

$$2\hat{d}_{xy} = B_{2I}\hat{v}_{xI} + B_{1I}\hat{v}_{yI} + \hat{z}\left(B_{2I}\hat{\theta}_{yI} - B_{1I}\hat{\theta}_{xI}\right) \tag{1.45}$$

$$2\hat{d}_{xz} = B_{1I}\hat{v}_{zI} + N_I\hat{\theta}_{yI} \tag{1.46}$$

$$2\hat{d}_{yz} = B_{2I}\hat{v}_{2I} - N_I\hat{\theta}_{xI} \tag{1.47}$$

where

$$B_{1I} = \frac{\partial N_I}{\partial \hat{x}} \tag{1.48}$$

$$B_{2I} = \frac{\partial N_I}{\partial \hat{y}} \tag{1.49}$$

After evaluating the velocity strain components, the force and moment resultants are given by (*LS-DYNA Theory Manual,* 2006):

$$\hat{f}^R_{\alpha\beta} = \int \hat{\sigma}_{\alpha\beta} d\hat{z} \tag{1.50}$$

$$\hat{m}^R_{\alpha\beta} = -\int \hat{z}\hat{\sigma}_{\alpha\beta} d\hat{z} \tag{1.51}$$

where the superscript R indicates a resultant force or moment, the Greek subscripts emphasize the limited range of the indices for plane stress plasticity, $\hat{f}^R_{\alpha\beta}$ is the force resultant, $\hat{m}^R_{\alpha\beta}$ is the moment resultant, and $\hat{\sigma}_{\alpha\beta}$ is the corresponding stress.

The relations between the above element-centered forces and moment resultants and local nodal forces and moments are given by (*LS-DYNA Theory Manual,* 2006):

$$\hat{f}_{xI} = A\left(B_{1I}\hat{f}^R_{xx} + B_{2I}\hat{f}^R_{xy}\right) \tag{1.52}$$

$$\hat{f}_{yI} = A\left(B_{2I}\hat{f}^R_{yy} + B_{1I}\hat{f}^R_{xy}\right) \tag{1.53}$$

$$\hat{f}_{zI} = A\kappa\left(B_{1I}\hat{f}^R_{xz} + B_{2I}\hat{f}^R_{yz}\right) \tag{1.54}$$

$$\hat{m}_{xI} = A\left(B_{2I}\hat{m}^R_{yy} + B_{1I}\hat{m}^R_{xy} - \frac{\kappa}{4}\hat{f}^R_{yz}\right) \tag{1.55}$$

$$\hat{m}_{yI} = -A\left(B_{1I}\hat{m}^R_{xx} + B_{2I}\hat{m}^R_{xy} - \frac{\kappa}{4}\hat{f}^R_{xz}\right) \tag{1.56}$$

$$\hat{m}_{zI} = 0 \tag{1.57}$$

where A is the area of the element, κ is the shear factor from the Mindlin (1951) theory. Following equation (1.27), the above nodal forces and moments can be transformed to the global coordinate system.

1.8 Objective of the thesis

Based on finite element simulation, this thesis seeks to evaluate some innovative tube fitting forming processes. Validating with experimental results and theory, this thesis gives an instructive orientation for tube hydroforming and tube push-bending.

Chapter 1 is the introduction of several industrial fittings (T and Y tube joints and bent tubes), and innovative methods for their manufacture.

Chapter 2 deals with T-hydroforming, followed by a set of FEM simulations, and a discussion of the results. A figure for the theoretical working ranges, which contains several important curves, is validated by the FEM results.

Chapter 3 also deals with hydroforming, but focuses on Y-joints and contains a literature survey of Y-hydroforming. Differing from Chapter 2, thickness changes in tubes blanks due to forming are the main consideration.

Chapter 4 focuses on the simulation of a new tube bending method – tube push-bending. The advantages of this method mentioned earlier are demonstrated by a series of FEM simulations. Also some theoretical work is presented to validate the FEM simulations.

In Chapter 5, conclusions are presented and some suggestions are made for further research.

Chapter 2
T-Hydroforming

2.1 Literature survey

T-joints (figure 1.1) are used extensively in the pressure vessel industry. A number of studies have been published dealing with the simulation of the hydroforming of T-joints. The recent work is focused on the finite element method (FEM), and is built on earlier studies on hydroforming dating back to the 1980s (Koc, 2001). With the increase of computer power the finite element models have evolved from relatively crude approximations to more detailed ones, covering many factors affecting the process.

In 2000, three studies on the hydroforming of tees appeared, respectively by MacDonald and Hashmi (2000), Hsu and Lei (2000), and Koc *et al.* (2000). In the first of these studies, two different types of loading were considered, and the effects of friction and tube thickness were examined. Information was provided about the deformation, stresses, and tube thinning/thickening. Both the die and tube were modeled with eight-node solid elements. The mesh contained 1435 elements, 1140 of which described the tube. In the study by Hsu and Lei (2000), a simplified analytical model was proposed to predict material flow and fracture during forming. An industrial case was discussed, and good agreement between the FEM and the proposed analytical model was obtained. In the study by Koc *et al.* (2000), the focus was on preparing design guidelines that relate to

maximizing part expansion.

In the period 2001 to 2003, three further studies on T-hydroforming appeared, respectively by Lei *et al.* (2001, 2002), and Wu and Huang (2003). In the first of these, i.e. Lei *et al.* (2001), a three-dimensional FEM program based on the rigid-plastic model was introduced. The simulation results provided detailed information about the metal flow during the forming process, allowing for the formulation of a better design strategy for the forming. In the second study, i.e. Lei *et al.* (2002), the region of fracture initiation and the forming limits for tee extrusion were predicted. It was shown that the material parameters used in the ductile failure can be obtained from the experimental forming limit diagram. In the study by Wu and Huang (2003), adaptive techniques were used in the numerical process to improve the simulation. Tube hydroforming processes under a heat treatment were also studied.

Four studies published in 2004-2005 produced further information about the hydroforming of tees. Ray and Mac Donald (2004) focused on the optimization of the forming load path. They suggested the use of a fuzzy logic control algorithm in conjunction with a three-dimensional FEM code. In the study by Lin and Kwan (2004) the emphasis was on the fulfillment of requirements for wall thickness and protrusion height. The FEM was used to investigate the material flow characteristics under different process parameters, and the abductive network was then applied to synthesize the data sets from the numerical simulation to produce a predictive model. Abrantes *et al.* (2005) gave a report on a number

of aspects of the hydroforming of tees, including consideration of free bulging. Experimental results illustrating unsuitable forming load paths were presented, and a diagram indicating the process window was given. Ray and Mac Donald (2005) reported on FEM and experimental results for tees. Predicted values from the FEM simulation for wall thickness distribution and developed branch height were in good agreement with experimental results.

In 2007, new papers were published in the T-hydroforming field. Loukus *et al.* (2007) conducted FEM simulations of tube hydroforming for W-temper and T4 heat-treated condition by LS-DYNA. They found that hydroforming in the W-temper facilitates forming of a larger tee branch (due to available greater ductility), but limits the strength (hardness) of the final component compared to that formed in the T4 condition.

In this chapter, a shell-theory explicit finite element simulation of the hydroforming process for a T-joint is presented. The mesh comprises a rigid die, and a blank that is modeled as an elastic-plastic cylindrical shell, closed at the ends. Details of the numerical analysis are presented, including a description of the software used, and the main steps of the analysis. The importance of the correct combination of axial feed rate and pressure is indicated, and the working range in the pressure-axial feed interaction diagram is determined for some sample tee geometries. Furthermore, the working range in the pressure-axial force interaction diagram is made for two cases. The study is intended to provide information that is useful for designers of the T-joint fabrication process.

2.2 Theoretical analysis

Based on the theoretical interaction diagram (figure 2.1), there are 5 different fabrication outcomes, depending on the ranges of internal pressure and axial feed. They are respectively sealing range, elastic range, working range, bursting range and buckling range. Differing from the other ranges, the sealing and elastic ranges are pure elastic problems.

Bursting will take place when the material reaches its tensile strength. According to the shell membrane formula, the hoop stress σ_h can be expressed as (Bai, 2001):

$$\sigma_h = \frac{p \cdot r}{t} \tag{2.1}$$

where p is the internal pressure, r is the radius of the tube's cross-section, and t is the wall thickness of the shell.

If the ultimate stress of the material is known, the internal pressure which is needed to break the tube can be evaluated by using equation (2.1). However, in LS-DYNA, there is not an ultimate stress parameter that can be set to predict such material failure. Instead of an ultimate stress, the failure strain is an important parameter to detect the material failure. Once the strain of an element exceeds this failure strain, the solver will delete this element. In order to determine the ultimate strain, a bilinear elastic-plastic material model is employed, for the sake of simplicity (figure 2.2). Strains can then be obtained by the following equation:

$$\varepsilon_u = \varepsilon_y + \Delta\varepsilon \tag{2.2}$$

where ε_1 is the yield strain, and ε_2 is the strain increment from the yield point to the ultimate point. We can evaluate the ε_u by:

$$\varepsilon_u = \frac{\sigma_y}{E} + \frac{\sigma_u - \sigma_y}{E_t} \tag{2.3}$$

where σ_y and σ_u are the yield and ultimate tensile stresses respectively, E is the Young's modulus, and E_t is the tangent modulus, which describes the strength of a material beyond its yield point. Using these formulas, a theoretical straight line can be made as the bursting prediction.

2.3 Finite element models

The schematics and basic geometry for tee hydroforming are shown in figure 2.3. A high pressure liquid (water) is injected into the tube blank, which is sealed by two contacting dies. The tube blank is placed into a T-shaped die. The blank (cylindrical tube) has an external diameter of D_1, a length of L, and a thickness of t. The die cavity, corresponding to the position of the nozzle, has a diameter of D_2 and a height of H. The internal pressure applied to the blank is p, and the axial force is F. In a displacement controlled process the total axial feed is given by displacements. The parameters of three geometric cases considered for simulation in the current study are given in Table 2.1.

The internal pressure and axial feed are functions that depend on time. Their relation is crucial for a satisfactory product as seen in figure 2.1. For low pressure and high axial force, wrinkling or buckling can occur. For excessive pressure, bursting or fracture of the

blank in the area of the evolving nozzle can take place. A minimum axial force is required for sealing purposes. There is thus a limited working range, representing satisfactory combinations of axial effect and internal pressure to prevent failure of the specimen. Additional requirements may exist to obtain a satisfactory product.

Both the blank and the die were meshed with 4-node 24-degree-of-freedom shell elements. The die was treated as a rigid surface, while the tube was treated as a deformable solid. For the tube the element was based on the Belytschko-Lin-Tsay model, which contains a combined co-rotational and velocity-strain formulation. Using such algorithm, locking never took place during simulation. The element is efficient due to the mathematical simplifications that arise from the kinematic assumptions.

The material properties (Wu, 2003 and *Structural Alloys Handbook,* 1996) (Table 2.2) used in the simulation corresponded to AA6063-T6 aluminum with E=65.0 GPa, ν=0.28, K=181.0 MPa, n=0.318, σ_u=241.0 MPa, where E and ν are the Young's modulus and Poisson's ratio, K and n are material constants, i.e., the strength coefficient and hardening exponent, and σ_u is the ultimate strength of the material. AA6063 is a widely used aluminum alloy because of its excellent extrudability; it is the first choice for many architectural and structural members. AA6063 is used in many engineering applications such as bridges and highway structures, automobile frames, marine structures and ships, pressure vessels and pipelines. It is also a widely used material in hydroforming.

To reduce the model size, symmetry in the initial geometry was taken into account.

One half of the geometry was modeled (figure 2.4). An automatically generated mesh is a feature of the FEMB software, and this mesh was modified by LS-DYNA during the solution process to represent the major change in the shape of the tube around the evolving nozzle. The die was provided with a coarser mesh (about 1000 elements), while the tube was given a finer mesh (about 2000 elements). The die, treated as a rigid surface, had all nodes completely restrained. The blank, treated as a deformable solid, had symmetry conditions enforced on shell mid-surface lines of symmetry. The conditions of zero normal displacement, and zero rotation about two axes were enforced on the symmetry lines, representing the top and bottom lines of a vertical longitudinal section of the blank. The contact between blank and die was modeled as a surface contact with a coefficient of friction of 0.05 (Wu, 2003). It is found that larger coefficient values may lead to wrinkling. It is necessary to keep this value at a small level. At the right end of the blank a uniform horizontal axial displacement w to the left was specified. The left end of the blank was kept fixed. On the inner surface of the tube a uniform pressure p was specified. The loading was specified over a nominal 18- second period, and the time step, selected within the software was 0.0137 sec.

2.4 Simulation results

The main output of the simulation was the figure representing the deformed blank, now having the form of a closed T-joint. Observation of the result is a subjective process, but with sufficient resolution deformities in the product can be identified. Of particular

interest are wrinkles, fracture lines, fillet defects, and incomplete forming. An example of a satisfactory product is shown in figure 2.5, while unsatisfactory products are shown in figures 2.6 and 2.7. The defective products have respectively a fillet defect, resulting mainly from an excessive axial displacement, and incomplete forming, resulting mainly from an insufficient axial displacement.

Furthermore a set of simulations to illustrate bursting and buckling failure prediction were made. Figure 2.8 shows a buckling failure at the bottom of the tube product. Figure 2.9 shows a bursting failure on the top of the emerging nozzle.

The results of the study for the three geometric cases (Table 2.1) will be discussed. The first case concerns a thin-walled tee, and with the D_1 / D_2 ratio equal to 1. The second case concerns a thicker tee, and the D_1 / D_2 ratio again equal to 1. The third case concerns a thin-walled tee, with a D_1 / D_2 ratio of about 3/2.

In the simulations carried out in this study, the control of the axial displacements rather than the axial force provided greater numerical stability. The process was then described with a modified interaction diagram as shown in figure 2.10. For excessive internal pressure the hoop stress in the blank will reach the burst strength, and failure will occur.

For insufficient internal pressure, wrinkling or buckling can occur. If the axial displacement is too large, fillet defect takes place. On the other hand if the internal pressure or axial displacements are insufficient, an incomplete shape will be produced. Simulations

were carried out for the three geometric cases of Table 2.1 for different specified final internal pressure and axial displacement. The objective for each case was to establish a tentative working range diagram. The results obtained for the interaction diagrams for the three cases are given in figures 2.11-2.13. It is emphasized that these figures have been constructed solely through numerical simulations.

For case 1, the bursting pressure is about 20 MPa. The pressure for incomplete forming, giving a result similar to figure 2.7, is about 15 MPa. If the axial displacement exceeds about 60-70 mm a fillet defect, similar to that shown in figure 2.6, occurs. Furthermore if the axial feed is too small, less than about 40mm, an incomplete shape is obtained. By a series of simulations a working range as shown by the shaded area of figure 2.10 was developed. The area thus represents combinations of final axial displacement and internal pressure that lead to satisfactory forming.

For case 2 a similar diagram was established (figure 2.12). For this thicker shell there is a shift of the working range upwards, and to the right. The pressure range now is about 27-35 MPa, and the maximum axial feed between about 55-75 mm. This trend appears qualitatively correct in view of the thicker, stronger blank for this case.

For case 3, representing the thin shell with a diameter ratio D_1 / D_2 greater than one, the pressure range is between 20 and 30 MPa, and the maximum axial displacement between 65 and 75 mm (figure 2.13). Relative to case 1, which represents a tee with lower diameter ratio of D_1 / D_2, greater axial displacement and pressure are required.

Two further interaction diagrams (figure 2.14 and 2.15) are presented, in which the vertical axes represent axial forces rather than axial displacements. If a hydroforming machine has an axial force detector, it can be controlled by axial force instead of axial displacement. Figure 2.14 presents the simulation results for case 1. Comparing with figure 2.1, it is seen that the buckling failure points closely match the curve in figure 2.1. The bursting failure points are close to the theoretical bursting line. The working range can be considered as the area below the buckling points and to the left of the bursting line. Comparing figures 2.14 and 2.15, it is seen that case 2 has a higher force carrying ability than case 1, which is because the tube in case 2 has a higher wall-thickness than case 1.

The finite element simulations presented have instructive industrial meaning, although the working ranges are chosen by limited simulations. It is noted that the working ranges are closed by four straight lines. It is advisable to arrange for load combinations in the central area of the working range, to ensure a satisfactory product without a failure problem.

2.5 Conclusions

LS-DYNA is suitable to predict the working ranges for different T-hydroforming cases. The T-hydroforming needs a well-selected loading path: i.e. appropriate combinations of axial feeds and internal pressure. Inappropriate selection of loading paths leads to defective products. Using the finite element approach to determine the loading paths is effective and economical.

Chapter 3
Y-Hydroforming

3.1 Literature survey

Many researchers have made efforts to build analytical models for T and Y hydroforming. Nader (1999) presented an analytical model of general tube hydroforming, and predicted the successful working range for a good product. Optimization is a frequent research topic for hydroforming. Aue-U-Lan *et al.* (2004) used a finite element based method to determine the optimum loading paths for tube hydroforming. Kwan and Lin (2003) studied T-joint hydroforming using only FEM simulation without experiments, and selected the software DEFORM-3D. They found proper combinations of forces and pressure to get acceptable minimum wall thickness. Zhang and Redekop (2006) built a finite element model to validate the analytical model presented by Nader (1999). They predicted appropriate ranges of internal pressure and punch feed combinations for different geometry of the tube blank and the die.

There have been relatively few Y-joint studies to date. Jirathearanat *et al.* (2004) conducted experiments and did FEM simulation for Y-joint hydroforming, estimating optimum manufacturing parameters through FEM simulations.

A series of FEM models for Y-hydroforming are discussed in this chapter. The FEM procedure used is validated by comparing results with previous work. Suitable loading

paths for the various models are determined. Consideration is given to joints having angles ranging from 60 to 90 degrees. The chapter ends with conclusions about the characteristics of the FEM simulation and the hydroforming process.

3.2 Theoretical analysis

Bursting is a classical failure in hydroforming. It takes place in the form of a ductile fracture. Unlike brittle fracture, in ductile failure, extensive plastic deformation takes place before fracture. Based on various hypotheses, many criteria for ductile fracture have been proposed. Takuda *et al.* (1999) compared several existing fracture criteria with FEM simulations and experiments.

Lei *et al.* (2002) employed Oyane's (1980) ductile fracture criteria to predict bursting in T-hydroforming. In this chapter, Oyane's (1980) ductile fracture is employed to predict bursting in Y-hydroforming. Oyane's ductile fracture criterion assumes that the history of hydrostatic stress (mean stress) and equivalent stress affect the occurrence of the ductile fracture. The criterion is defined with regard to the relation:

$$\int_0^{\bar{\varepsilon}_f} \left(\frac{\sigma_h}{\bar{\sigma}} + C_1 \right) d\bar{\varepsilon} = C_2 \tag{3.1}$$

where $\bar{\varepsilon}_f$ is the equivalent strain at fracture, $\bar{\varepsilon}$ is the equivalent plastic strain, σ_h is the hydrostatic stress, $\bar{\sigma}$ is the equivalent stress, C_1 and C_2 are material constants. C_1 and C_2 can be determined by a uniaxial tensile test and a plane-strain tensile test. In this chapter, the properties of the aluminum AA5052-O are used in the bursting prediction. The

material constants for this alloy were given by Takuda *et al.* (1999). In their study, C_1 and C_2 were approximately evaluated at the values of 0.30 and 0.28 respectively. The mechanical properties for AA5052-O can be found in Table 2.2.

Equation (3.1) can be transformed as:

$$I = \frac{1}{C_2} \int_0^{\bar{\varepsilon}_f} \left(\frac{\sigma_h}{\bar{\sigma}} + C_1 \right) d\bar{\varepsilon} \tag{3.2}$$

Fracture is considered to occur when the ductile fracture integral, i.e. I, reaches unity. FEM simulations were carried out for the ductile fracture analysis. Data files from LS-DYNA were imported to the program "cal_ductile_int.m" and the integrations were numerically evaluated. The listing of this program, and others developed in this work, is given in Appendix B.

Following the definition of hydrostatic stress and equivalent stress (von Mises stress) in section 1.4, those stresses were evaluated in the programs "cal_von_mises_stress.m" and "cal_ductile_int.m" by reading the stress tensor components at a certain shell element. Three-point numerical integration was then employed to calculate the integral I for this element at any time step. The simulation results are discussed in section 3.5.

3.3 Finite element analysis

The determination of the load path is significant for satisfactory Y-hydroforming. Basically, there are two main loadings in Y-hydroforming: axial feeds, and internal pressure. In T-hydroforming, the loading path is easier to determine than in

Y-hydroforming, because in T-hydroforming, the two axial feeds are always the same. However, in Y-hydroforming, the axial feeds for the two punches are different (see figure 3.1). A non-unity ratio of those feeds must be considered in Y-hydroforming. An inappropriate value of this ratio may lead to incomplete forming or to a fillet defect. Due to the asymmetry, Y-hydroforming needs a stricter standard for choosing the internal pressure than T-hydroforming.

Figure 3.1 shows the geometric parameters and loading parameters for Y-hydroforming. D_0 is the diameter of the tube, D_1 is the diameter of the protrusion part, t is the thickness of the tube, and θ is the angle between the protrusion axis and the initial tube axis. In this thesis, we initially set θ=60°. Internal pressure p is used to support the shape of the tube. Displacements d_L and d_R are the axial feeds on the left and right hand sides of the tube, respectively.

Figure 3.2 shows the model built by SolidWorks (Model 1). A fillet radius of 10mm was assigned between the nozzle part and the blank part of the die.

Seven finite element models are built by FEMB, with different combination of material wall-thickness t, tube initial diameter D_0, and protrusion diameter D_1. The tube length in all cases is 500 mm (Table 3.1).

Figure 3.3 shows the model for FEM analysis. In this case, a fine mesh was used, 7mm element size for the tube, 10 mm element size for the die. A convergence study was carried out (see section 3.5). This study showed that a mesh of 10 mm size was suitable for

this problem. There is no doubt that a finer mesh would give a better result, but time cost per run was a consideration. Generally, in order to obtain a satisfactory result, tens of runs are needed for each model. With the current fine mesh (10mm), every run took more than 10 minutes with LS-DYNA 970 (running on a computer with a P4 2.4 GHz processor and 1GB memory units).

A surface-to-surface contact element was assigned between the tube and die parts. A friction coefficient of 0.05 (the same as in T-hydroforming simulation) was selected to simulate the lubrication condition.

The internal pressure and axial feed are functions of time. Axial feed (displacement) was increased linearly, while the internal pressure was increased to the maximum value quickly, and kept constant at this level until the end of the forming process. Figures 3.4 and 3.5 show the assigned internal pressure and axial feeds vs. time; the values shown are for model 2.

Choosing a proper load path is important for Y-hydroforming. For low pressure and high axial feed, buckling (figure 3.6) will occur. A low internal pressure also leads to an incomplete protrusion. So, the incomplete products often also contain buckles (figure 3.7). There is another unsuccessful forming which is called a fillet defect. If the axial feeds are the same for both sides, i.e. $d_L = d_R$, or they are chosen at an inappropriate ratio, the simulation always ends with a fillet defect (figure 3.8). It is because the lengths of the two side of the protrusion part is not the same; from figure 1.2, it is seen that the length on the

left hand side is smaller than the right hand side. To avoid this defect, d_L should be kept smaller than d_R. For example, a d_L / d_R ratio of 0.4~0.6 is an acceptable value for the tube with a 60° protrusion angle. Table 3.2 shows the loading paths for all models defined.

Three models each with different angles are built to study the protrusion of the Y-joint. The angles, 60°, 75° and 90° are considered. During the angular parametric study, it was found that it is difficult to obtain a satisfactory product with a 45° protrusion angle. So the minimum angle considered in this study is 60°.

3.4 Simulation results

FEM simulations were carried out for a validation study. Experimental results from Jirathearantat (2004) were used for comparison. An FEM model was built with $D_1 = D_2 = 50.5$ mm, thickness $t = 1.5$ mm, and the material SS304 steel was employed. The material properties for SS304 were those of Table 2.2. The extreme thinning thickness is 1.06 mm from the FEM simulation, compared to 1.13 mm in their experiment; the error is less than 7%.

In order to check the convergence of the FEM models, a convergence study was carried out for model 1. The size of the elements for three different meshes are respectively 15 mm, 10 mm and 7 mm for the tube part, corresponding to a coarse mesh, a medium mesh, and a refined mesh. Using post-process software, four types of results were observed: thinning, thickening, maximum von Mises stress, and plastic strain. From Table 3.3, it is seen that the results converged very well as the mesh is refined.

Figure 3.9 gives the thickness distribution for model 7. A counter punch was used in this simulation. The area with most thinning is at the top of the protrusion part. The thickness changes from its original value 1.50 mm to 0.67 mm (44.7% left). The area with most thickening is at the fillet area, which is under high compression during the forming process; the thickness increases to 2.04 mm from 1.50 mm (136.0%).

Figure 3.10 shows the maximum von Mises stress distribution for model 7. From the simulation result, it is clearly seen that the maximum value of this stress is at the top of the protrusion, reaching a value of 299.78 MPa. This stress level is reasonable comparing with simulation results from Loukus (2007).

Figure 3.11 shows the plastic strain distribution for model 7. The maximum plastic strain is located near the fillet area, where buckling easily occurs.

Figure 3.12 gives a plot of the thickness distribution on the longitudinal section for model 7. This figure indicates that the minimum thickness is located near the mid-point at the top of the protrusion. The thickness is asymmetrically distributed. The maximum thickness is at the right hand side of the protrusion. The thickness distributes conically on the protrusion part.

Table 3.4 gives results for the seven FEM models of the parametric study. From this table and the model definitions, several conclusions can be made. 1) The thinning percentage is greater when the thickness of the tube is smaller. Of the models 1, 2 and 3, model 1 has the smallest wall-thickness 0.89 mm, but has the minimum thickness

remaining. Model 3 has the largest wall-thickness, but it has the minimum thinning. The thickening has the reversed trend. It is larger when the thickness of the tube is larger. 2) The maximum von Mises stress increases when the wall thickness decreases, but not greatly so. However, the maximum von Mises stress is much smaller in model 4, which has a smaller diameter of the protrusion. 3) The maximum plastic strain is wall-thickness sensitive. In models 1, 2, and 3, it decreases from 0.87 to 0.84 as the thickness decreases from 1.65 mm to 0.89 mm. Greater thickness leads to higher maximum plastic strain. 4) Tubes with greater protrusion diameter have higher thinning. But the thickening change is not obvious. Also, the plastic strain is a little lower than ones with larger protrusion diameter. 5) For the tubes of steel SS304 alloy, there is less thinning than for tubes with aluminum alloy. Because of the high strength coefficient and high hardening exponent for steel alloy, the maximum von Mises stresses found in models 5 and 6 are much higher than models 1 to 4. In the parametric study, a counter punch was employed and simulated to make sure the protrusion part was fully expanded. Unlike simulations for validation and angle parametric study, these simulations lead to a more intense thinning and thickening. Such phenomenon takes place because the protrusion part expanded more and the lower tube part compressed more.

Several FEM models were built for the angle parametric study. Table 3.5 gives the model definitions with different protrusion angles. The loading paths are given in Table 3.6. It should be noted that the values for d_L have large changes as the angle varies. The ratio

of d_L / d_R should be increased as the angle increases. Figures 3.13 - 3.15 give the simulation results for different Y-angles. Table 3.7 gives the results for thickness changes and maximum von Mises stress for the three models. As the angle between protrusion and initial tube blank increases, it is seen that the trend of thinning in the top of the protrusion area decreases (from 55.5% to 73.9%), while the trend of thickening increases (from 119.2% to 130.0%). The maximum von Mises stresses do not show an obvious trend.

A prediction of bursting for Y-hydroforming was made in this study. Four specific elements of mesh were selected for model 7 (figure 3.16). Following the method mentioned in section 3.3, the ductile fracture integrals I_1 - I_4 were evaluated corresponding to the elements 1-4 with the results; $I_1 = 1.4227$, $I_2 = 1.1433$, $I_3 = 0.6442$, and $I_4 = 0.7775$. Because I_1 and I_2 exceed 1, ductile fracture will take place at elements 1 and 2, at the current time step. In order to determine the earliest time stage when bursting occurs, figure 3.17 was generated. This figure shows the change of ductile fracture integration with the time, for element 1. It is seen that at the time of about 25 ms, the integration reaches 1, indicating that bursting takes place at time 25 ms.

3.5 Conclusions

The hydroforming of Y-joints needs a well-selected loading path: axial feeds and internal pressure. Selection of an inappropriate loading path leads to an unsuccessful product. In order to determine the loading parameters, FEM analysis is convenient and economic compared to experimental trial-and-error efforts. Previous work has shown that

the results of FEM simulation agree with experimental results. The forming plan for a satisfactory product can be easily prepared using the FEM approach. The ductile fracture criterion is very useful in FEM for the prediction of bursting. Finally the FEM approach is convenient to predict thickness change, stresses, and bursting which are important factors affecting bursting failure.

Chapter 4
Tube Push-Bending

4.1 Literature survey

The pipe forming industry is facing the challenge of modernizing production methods in the fabrication of curved tubes (elbow sections). Component costs need to be reduced, and component properties need to be improved. The costs can be reduced by increasing production rates and reliability, while properties can be improved by using better forming methods. So there is a need to develop new manufacturing techniques, which give an improvement over existing methods (Tang 2000).

The push-bending process (figure 4.1 - 4.2), which features the use of an elastomer rod to prevent buckling and to keep the cross section's shape of the tube during forming, has been proposed recently (Zhang and Redekop 2006, Baudin *et al.* 2004, Zeng and Li 2002, Al-Qureshi 1999) as offering significant improvements over existing methods.

Zhang and Redekop (2006) have described a finite element method (FEM) simulation, based on shell elements, of this process of tube bending. An internal pressure was used to represent the effect of the elastomer rod to reduce wrinkling. Yang and Lin (2004) developed an analytical model for predicting wrinkling in tube bending. In an earlier work Baudin *et al.* (2004) had used a three-dimensional element approach, in which the rod was explicitly modeled. The solution of a double contact problem in their work led to some

numerical difficulties for some cases.

The objective of the current study is to provide further data concerning the push-bending process. Further work using the shell element simulation of the process, retaining the internal pressure approximation, has been carried out. Additional aspects of the process, such as spring-back, material waste, maximum forming load, were included in the present study. A convergence and validation study was conducted to ensure conformity with previous work. Finally, a parametric study was carried out, giving results for a number of choices for the forming process.

4.2 Theoretical basis

In the FEM simulation the material is modeled as plastic, with kinematic hardening. Because the tube is formed at a cold temperature, a work hardening factor should be considered. Work hardening occurs when a metal is strained beyond the yield point. An increasing stress is required to produce additional plastic deformation and the metal apparently becomes stronger and more difficult to deform. If true stress is plotted against true strain, the rate of strain hardening tends to become almost uniform, that is, the curve becomes almost a straight line (figure 4.3). With kinematic hardening the yield surface will shift as a function of plastic strain without changing shape or size.

4.3 Spring-back

Spring-back is a phenomenon that occurs when a flat-rolled metal or alloy is cold-worked; upon release of the forming force, the material has a tendency to partially

return to its original shape because of the elastic recovery of the material. Spring-back is influenced not only by the tensile and yield strengths, but also by thickness, bend radius and bend angle.

Spring-back commonly occurs in metal stamping and sheet forming (Lei *et al* 2004), but it can also take place in tube push-bending process. The evaluation of the spring-back factor for tube push-bending is important. It helps to determine if the product is in accord with the tube bend tolerances or not. Generally, the angle of the tube product is always larger than the angle of the die. In the current research, the spring-factor is calculated and simulated for several bending cases.

For the analysis of the spring-back the material was assumed to be elastic-perfectly plastic. Prior to spring-back it was assumed that the whole tube had been loaded into the plastic range. A cross-section of the tube is shown in figure 4.4, in which r_2 and r_1 are the inner and outer radii of the tube. The theory presented is based on previous work (Al-Qureshi 1999, 2002, Timoshenko 1958, Nguyen *et al.* 2004). The moment at yield, M_{YP} is given by:

$$M_{YP} = \sigma_0 I_z \frac{1}{r_1} \tag{4.1}$$

where σ_0 is the yield stress, and I_z is the second moment of area with respect to the axes along the neutral line. The ratio of the moment at ultimate (fully plastically deformed on the cross-section of the tube) to the moment at yield is given by Timoshenko (1958) as:

$$\frac{M_{ult}}{M_{YP}} = \frac{16r_1}{3\pi} \cdot \frac{r_1^3 - r_2^3}{r_1^4 - r_2^4} \tag{4.2}$$

Thus, the moment at ultimate can be expressed as:

$$M_{ult} = \frac{16r_1}{3\pi} \cdot \frac{r_1^3 - r_2^3}{r_1^4 - r_2^4} \cdot \frac{\sigma_0 I_z}{r_1} \tag{4.3}$$

The moment at ultimate is also given by Al-Qureshi (1999) as:

$$M_{ult} = (\frac{1}{\rho_0} - \frac{1}{\rho_f}) EI_z \tag{4.4}$$

Therefore,

$$\frac{\rho_0}{\rho_f} = 1 - \frac{M_{ult}\rho_0}{EI_z} = 1 - \frac{16(r_1^3 - r_2^3)\sigma_0\rho_0}{3\pi E(r_1^4 - r_2^4)} \tag{4.5}$$

where ρ_0 is the initial bending radius (central line), ρ_f is the final bending radius (central line), and E is the Young's modulus. The ratio ρ_0/ρ_f given in (4.5) is referred to as the spring-back factor, which is indicative of the spring-back upon release of the tube from the die constraint.

To validate the spring-back theory, a comparison for four geometric-material cases is given in Table 4.1. Two different types of aluminum alloys are represented. Four different formed radii of curvature ranging from 25 to 152.4 mm are considered. The results for the spring-back factor, obtained by the theory presented in the present study, and in a previous experiment (Al-Qureshi and Russo 2002), are given in the last two rows of the table. The differences in the respective values are less than 2%.

4.4 FEM modeling of the forming process

The geometry of the model was developed using the SolidWorks software. Shell elements rather than 3D elements were used, to reduce the problem size. The non-linear elastic-plastic material model used in the simulation was taken as rate-independent, as the overall duration of the forming process is relatively long. Of the two strain rate independent plasticity models available in LS-DYNA the classical bilinear kinematic hardening model was used in the present study. An automatic surface-to-surface contact algorithm was employed for the interface between the die and the tube. The value of 0.1 was assigned for the coefficient of friction for the die-tube contact. Higher friction coefficient requires higher axial load. It is necessary to have a good lubrication condition, which means the coefficient value should be kept smaller than 0.1.

The simulations were carried out for a 90^{o} bend of a straight tube of about 40-50 mm outer diameter, 1-2 mm thickness, and a length of about 140-200 mm. The die had a cross-sectional inner radius of 40-50 mm and a die bend radius of 40-70 mm.

The die, modeled as a rigid body, and the tube, modeled as an elastic-plastic body, were provided with constraints at the nodes on the plane of symmetry. The specified loading comprised of a prescribed steadily increasing displacement, which was applied to the nodes at the free end of the tube. Figure 4.5 gives a plot of the axial feeds versus time for model V1. The axial displacement reaches 200 mm as the time increases to 200 ms. Because the reaction of elastomer rod under an external pressure is unknown, the

magnitude of the internal pressure was not treated as a parameter in this simulation. The value of 15 MPa was selected as a reasonable level to avoid wrinkling. As this pressure is used to simulate the mandrel that is placed in the tube blank, the mandrel has to be strong enough to provide that pressure level.

Sample finite element meshes representing the simulation before and after forming are shown in figures 4.1-4.2, while a sample stress-strain diagram is given in figure 4.3. For the finished tube three main cross-sections (A, B, and C), and two sides (extrados, intrados) are of interest (figure 4.6). Due to the nature of the forming process there will be material waste (figure 4.7). A major concern in the forming is the avoidance of wrinkles (figure 4.8) at the intrados. The axial force, which was computed from the program "calForceWithTime.m", in general did not have a steady increment. A typical force versus time graph is shown in figure 4.9. Figure 4.10 defines the cross-sectional angle θ, and figure 4.11 gives a curve for axial normal stress distribution with respect to that angle. It is seen that during forming, on the top of the cross-section elements are undergoing tension, while on the bottom elements are undergoing compression.

In order to evaluate the axial force that is needed for the forming machine, program "calForceWithTime.m" was written. The total axial force is calculated by summing the forces on all elements at the end of the tube. To calculate the force on an element, the stress along the forming direction should be evaluated. By multiplying the cross-sectional area of an element, the force on this element can be obtained. The program

"calForceWithTime.m" is used for extracting the element information from a text formed output file from one of LS-DYNA's post-processor and making calculations. Figures 4.9 and 4.11 are obtained by these programs.

To perform a spring-back simulation in LS-DYNA, a seamless spring-back interface was employed. Because the spring-back problems involve static analysis, an implicit linear method was employed in LS-DYNA, as opposed to the explicit non-linear method used to produce the deformed product.

4.5 Convergence and validation

To validate the current work comparisons were made with results from the study of Baudin *et al.* (2004). It is important to note the major differences in modeling between the two studies. In the earlier work, solid elements were employed to mesh both the tube and the elastomer rod, and the tube-rod interaction was treated as a contact problem. In the present work, thin shell elements were used to mesh the tube, and internal pressure was applied on the inner surface of the tube to represent the tube-rod interaction.

A description of the models used in the validation and convergence study is given in Table 4.2. Results are first given for the validation; model V1, i.e. a model with a tube having a bending radius of 70 mm. The material for the validation and parametric studies was assumed to be an aluminum alloy AA6063-T6 (see Table 2.2). In the parametric study, discussed in the following section, a mild steel material was also considered.

An indication of the convergence characteristics for model V1 is given in Table 4.3.

Results are presented for three mesh levels: i.e. coarse, medium, and refined. The coarse, medium and refined meshes were defined as ones having nominal element sizes of 10, 8, and 5 mm, respectively. The results given in the table are the final wall thickness, and the maximum von Mises stress at the intrados and extrados (B section). It is observed that there are relatively minor changes in the results in going from the medium to the refined mesh; however, a refined mesh was used to get the most accurate results.

A comparison of results obtained in the current study and in the study by Baudin *et al.* (2004) for model V1 is given in Table 4.4. The comparisons are for the wall thicknesses at the intrados and extrados of the three cross-sections A, B, and C of figure 4.6. Although different element types and different simulation methods were employed, the thickness distribution results are very close, all of the deviations being less than 10%. Because the material properties were not fully defined in the paper of Baudin *et al.* (2004), a comparison is not presented for the von Mises stresses.

4.6 Parametric study

To determine the effect of the geometry on results a parametric study involving eighteen models was carried out. The description of the models is given in Table 4.2. For the first nine models (the A models) the tube outside diameter (OD) was 41.27 mm, while for the last nine models (the B models) the OD was 50.80 mm. Three standard values (ASTM A-513) of the tube thickness were considered, 0.89 mm, 1.25 mm, and 1.89 mm. The bend radius was taken as a ratio of the outside diameter (ratio×OD), and ratios of 1,

1.5, and 2 were considered. In early advocacy for push-bending a relatively moderate bending radius (of around 2) was suggested, but in this study various radii are considered.

Results from the simulation, for final wall thickness and maximum von Mises stress at the extrados and intrados for the eighteen models are given in Table 4.5. Considering first the results for thickness it is seen that the values for the wall thickness for the A models are invariably higher than the corresponding values for the B models. This trend is observed regardless of the initial tube thickness, or the bending radius ratio. It must be pointed out though, that the radii of bends for the A models are considerably smaller than the radii of bends for the B models. A second trend that is generally observed is that the values for the wall thickness at the extrados are invariably less than the values for the initial thickness, while the values for the wall thickness at the intrados are invariably greater. This result follows naturally from the concepts of stretching and compressing of the axial lines of the tube when the bend is formed.

Considering next the effect of bend radius on final wall thickness it is seen that the values for the thickness corresponding to low bending radii are universally higher than values for high bending radii. It is observed that the decrease in wall thickness at the extrados is generally much smaller than the increase in thickness at the intrados.

The stress is an important consideration in the bending process. If in the tensile part the stress exceeds the ultimate stress of the material the tube will break. If in the compression part the stress exceeds the buckling stress wrinkles will form.

The maximum values for the von Mises stresses in Table 4.5 are unsigned, i.e. absolute values are given by the software. It is evident that the stresses at the extrados are tensile, and the stresses at the intrados are compressive. It is clear that any wrinkling that will occur will do so at the intrados. The stress level at the intrados is invariable higher than at the extrados. It is seen that for a given OD and a given bending ratio the stress levels increase moderately as the wall thickness increases. For a given OD and a given thickness the stress levels at the intrados decrease as the bending ratio increases and the stress levels at the extrados initially increase and then decrease. Furthermore, the maximum von Mises stress levels increase as the radius decreases.

Results from the simulation, for spring-back, material waste, and maximum axial load for the eighteen models are given in Table 4.6. It is seen that the original thickness does not affect strongly the results for the spring-back factor given by the theory or FEM. The FEM simulation results are somewhat smaller than analytical results; this may be due to the pure plasticity assumption in the theory. The factor which influences the spring-back significantly is the bending radius. As this radius is increased the spring-back increases (the value of spring-back factor decreases). The material waste decreases as the bend radius increases. If the bend radius is fixed, the material waste generally decreases as the initial thickness of the tube increases. The maximum axial load for different models has a large variation. For the models with the same bend radius, the maximum axial load increases as the initial thickness increases. The values for the B models are larger than those for the A

models (for the same bend radius level). However, when the bend radius changes for a fixed OD, the tendencies of the maximum axial load are not the same for the two sets of models. The reason is not apparent from the current theory.

All the results considered so far were for an aluminum alloy. In order to test the push-bending method for other materials, simulations were also carried out for steel tubes. Results for final wall thickness and maximum von Mises stress for a steel tube with a bend radius of 70 mm and wall thickness of 1.2 mm (Model V1) are given in Table 4.7. Considering the thickness, the smallest thickness of the steel tube is smaller than that of a comparable aluminum tube (Table 4.3). The largest thickness in the steel tube is greater than that of the aluminum tube. In this respect it is apparent that aluminum is better suited for the push-bending method than steel. Comparing the von Mises stress values with results in Table 4.3 it is seen that the von Mises stress in the steel tube is larger in the aluminum tube. This result is intuitive in that steel has a larger Young's modulus, and a higher yield stress than aluminum.

As the lubricant parameter also has an effect on the final thickness and maximum von Mises stress results, a simulation for lubrication with less favorable characteristics was carried out. The coefficient of friction was increased from 0.1 to 0.15. From the results, given in Table 4.8, it is seen that the wall thickness values have generally decreased, and the stress values increased relative to earlier values (Table 4.3). Clearly, a suitable level of lubrication is needed to obtain good forming results.

In a proper forming process for tubes the wrinkling will not occur. In the simulations carried out in this study it was found that the smaller the bending radius, the greater the likelihood of wrinkling. Figure 4.7(a) shows a simulation result of a formed tube where wrinkling did take place. To reduce or eliminate the wrinkling problem, a higher internal pressure should be applied or a longer forming time should be employed. The simulation result of figure 4.7 (b) corresponds to a higher internal pressure and a longer process time than that of figure 4.7 (a).

Due to the presence of various interacting parameters, care must be taken to plan a good, economical process. For small radius bending, as the radius is decreased a higher internal pressure is needed, which means that a higher Young's modulus is required of the elastomer rod. An increase in the allotted forming time of course decreases the quantity of the product, increasing the cost.

4.7 Conclusions

Several parameters affected the forming results; bending radius, material properties, friction coefficient, processing time. Bending radius was an essential parameter; as it decreased, many difficulties and obstacles appeared. Internal pressure was important because its effect was for withstanding the shape of the tube, and to reduce the winkling. Material properties were respectively important parameters for the forming, when steel alloy was used, thinner thickness was reached. The friction coefficient was a less important parameter, but when it exceeds 0.2, an undesirable shape will be produced, such as

wrinkling. It is better to keep it less than 0.15, which means good lubrication conditions are required. To eliminate wrinkling, the best way is to increase the internal pressure and the forming time.

Chapter 5
Conclusions

5.1 T-hydroforming

Based on the current work on T-hydroforming, a number of conclusions can be drawn. Suitable loading paths of T-hydroforming are essential to obtain satisfactory products. From figures 2.11 and 2.13, it is seen that, for different nozzle-pipe diameter ratios, different working ranges are found, and higher internal pressure is required when the diameter ratio increases. From figures 2.11 and 2.12, it is seen that, for cases of different wall thickness, different working ranges are found; the greater the thickness is, the greater the pressure that is required. Loading controlled by displacement is not as sensitive to such change; the pressure increases a little when the thickness increases.

Comparing figure 2.1 with figure 2.14 and 2.15, it is sent that FEM simulation results agree well numerically with theory in bursting prediction; buckling curves predicted by FEM simulations have similar shapes compared to the theoretical diagrams. However, the buckling points indicate a monotonic curve rather than the curve shown in the theoretical diagram.

5.2 Y-hydroforming

Based on the current study on Y-hydroforming, a number of conclusions can be drawn. Satisfactory hydroforming of Y-shapes needs a well-selected loading path. The

displacement loading paths for the two punches must be different; as the angle between the protrusion and the tube body decreases (assuming the angle is smaller than 90 degrees), the difference between the paths increases. The thinning becomes greater when the wall thickness of the tube becomes smaller (table 3.4). The maximum von Mises stress increases when the wall thickness decreases, but not significantly so. The maximum plastic strain is wall-thickness sensitive. It should be noted that, different results for one case may be obtained when loading paths are changed. In tables 3.4 and 3.7, the simulation results for case 2 have some difference. It is because the internal pressure applied for the two simulations are different (see tables 3.2 and 3.6). This phenomenon also proves that higher internal pressure leads to greater stress and higher thinning.

In addition to the asymmetric axial loading problem, another difficulty for Y-hydroforming compared with T-hydroforming is the thinning problem. From table 3.7, it is observed that the thinning for Y-hydroforming is greater than for T-hydroforming. The value for thinning is obtained by dividing the remaining thickness by the original thickness. The part with the most thinning for T-hydroforming (case 9) has only a 26.1% reduction in thickness, but for the 60 degree Y-hydroforming there is almost a 50% reduction.

For tubes of steel alloy SS304, the thinning is greater than for aluminum alloy, and the von Mises stress is much higher.

The Oyane's (1980) ductile fracture criterion is successfully used in FEM simulation for Y-hydroforming. Actually, such an approach is very suitable for combining FEM

simulations and specially written computer programs. FEM simulations may provide, at each time step, sufficient and overall numerical results which can be used by the computer programs to carry out integration.

5.3 Tube push-bending

Based on the current study on tube push-bending, the following conclusions are drawn. LS-DYNA with shell element is suitable for simulating the tube push-bending process. The bending radius is a significant parameter, as it decreases, many difficulties and obstacles appear. If the bending radius is too small (less than 1xOD), wrinkling can easily take place even at a high internal pressure, and sometimes the tube is blocked by the die, so it can not be successfully bent.

Internal pressure has the effect of reducing wrinkling. Without internal pressure (or with an internal pressure that is too low), there is wrinkling for all forming with no exception. This phenomenon indicates that the elastomer rod used in the industrial process should be stiff enough to provide sufficient pressure to support the wall of the tube.

Material waste and spring-bank are inevitable in tube bending, so the final length and final bent angle should be pre-evaluated before forming. From table 4.5, it can be observed that, at the extrados side, there is always thinning. Examinations should be carried out after forming to ensure good quality. The range of axial forces is large for different cases, so it is important to check the structural capacity of the forming machine.

5.4 Suggestions for further research

In hydroforming, further FEM simulation work could be conducted on more complex geometric problems, such as bellows hydroforming. Other ductile fracture criteria could be validated by FEM in a future study. In tube push-bending the current work has provided the simulation for wrinkling prediction by FEM simulations, further research could concentrate on wrinkling prediction by using shell bending theory, and comparison with current simulation results.

References

Abrantes J.P., Szabo-Ponce A., Batalha G.F., Experimental and numerical simulation of tube hydroforming, 8th Int. Conf. on Advances in Materials and Processing, COMMENT-05, Gliwice, Poland, 2005.

Al-Qureshi H.A., Elastic-plastic analysis of tube bending, International Journal of Machine Tools and Manufacture, Vol. 39, p 87-104, 1999.

Al-Qureshi H.A., Russo A., Springback and residual stress in bending of thin-walled aluminum tubes, Materials and Design, Vol. 23, p 217-222, 2002.

Aue-U-Lan Y., Ngaile G., Altan T., Optimizing tube hydroforming using process simulation and experimental verification, Journal of Materials Processing Technology, Vol. 146, p 137-143, 2004.

Bai Y., *Pipelines and Risers*, Elsevier, 2001.

Baker E.H., Kovalevsky L., Rish F.L., *Structural Analysis of Shells*, McGraw-Hill, Inc., 1972.

Bathe K.-J., *Finite Element Procedures*, Prentice Hall, Upper Saddle River, New Jersey, 1996.

Baudin S., Ray P., Mac Donald B.J., Hashmib M.S.J., Development of a novel method of tube bending using finite element simulation, Journal of Materials Processing Technology, Vol. 153–154, p 128–133, 2004.

Belytschko T., Tsay C.S., Explicit algorithms for nonlinear dynamics of shells, AMD, Vol. 48, ASME, p 209-231, 1981.

Hill, R., *The Mathematical Theory of Plasticity*, Oxford, Clarendon Press, 1950.

Hsu Q.C., Lei S.H., Development and analysis for the large-scale tee-forming process, Journal of Materials Processing Technology., Vol. 104, p 265-270, 2000.

Jirathearantat S., Hartl C., Altan T., Hydroforming of Y-shapes-product and process design using FEA simulation and experiments, Journal of Materials Processing Technology, Vol. 146, Issue 1, 15, p 124-129, 2004.

Koc M., Allen T., Jiratheranat S., The use of FEA and design of experiments to establish design guidelines for simple hydroformed parts, International Journal of Machine Tools and Manufacture, Vol. 40, p 2249-2266, 2000.

Koc M., Altan T., An overall review of the tube hydroforming (THF) technology, Journal of Materials Processing Technology, Vol. 108, p 384-393, 2001.

Kwan C.T., Lin F.C., Investigation of T-shape Tube Hydroforming with Finite Element Method, International Journal of Advanced Manufacturing Technology, Vol. 21, p 420-425, 2003.

Lee M.G., Kim D., Kim C., Wenner M.L., Chung K., Spring-back evaluation of automotive sheets based on isotropic-kinematic hardening laws and non-quadratic anisotropic yield functions, part III: applications, International Journal of Plasticity, Vol. 21, p 915-953, 2005.

Lei L.P., Kim J., Kang B.S., Hwang S.M., Kang B.S., Analysis and design of hydroforming processes by the rigid-plastic finite element method, Journal of Materials Processing Technology, Vol. 114, p 201-206, 2001.

Lei L.P., Kim J., Kang B.S., Bursting failure prediction in tube hydroforming processes by using rigid-plastic FEM combined with ductile fracture criterion, International Journal of Mechanical Science., Vol. 44, p 1411-1428, 2002.

Lin F.C., Kwan C.T., Application of abductive network and FEM to predict an acceptable product in T-shape tube hydroforming process, Computers and Structures., Vol. 82, p 1189-1200, 2004.

Loukus A.R., Subhash G., Imaninejad M., Optimization of material properties and process parameters for tube hydroforming of aluminium extrusions, Journal of Engineering Materials and Technology, Vol. 129, p 233-241, 2007.

LS-DYNA Theory Manual, Livermore Software Technology Corporation, 2006.

MacDonald B.J., Hashmi M.S.J., Finite element simulation of bulge forming of a crossjoint from a tubular blank, Journal of Materials Processing Technology, Vol. 103, p 333-342, 2000.

Structural Alloys Handbook, Purdue University-Cindas, 1996.

Mindlin R.D., Influence of rotary inertia and shear on flexural motions of isotropic, elastic plates, Journal of Applied Mechanics, Vol. 18, p 31-38, 1951.

Nader A., Analytical modeling of tube hydroforming, Thin-Walled Structures, Vol. 34, p 295-330, 1999.

Nguyen V.T., Cen Z., Thompson P.F., Prediction of spring-back in anisotropic shell metals, Journal of Mechanical Engineering Sciences, Vol. 218, p 651-661, 2004.

Oyane M., Sato T., Okimoto K., Shima S., Criteria for ductile fracture and their applications, Journal of Mechanical Working and Technology, Vol. 4, p 65-81, 1980.

Ray P., Mac Donald B.J., Determination of the optimal load path for tube hydroforming processes using a fuzzy load control algorithm and finite element analysis, Finite Element in Analysis and Design, Vol. 41, p 173-192, 2004.

Ray P., MacDonald B.J., Experimental study and finite element analysis of simple X and T-branch tube hydroforming processes, International Journal of Mechanical Sciences, Vol. 47, p 1498-1518, 2005.

Soedel W., *Vibrations of Shells and Plates*, Marcel Dekker, Inc., 1981.

Takuda H., Mori K., Hatta N., The application of some criteria for ductile fracture to the prediction of the forming limit of sheet metals, Journal of Materials Processing Technology, Vol. 95, p 116-121, 1999.

Tang N.C., Plastic-deformation analysis in tube bending, International Journal of Pressure Vessels and Piping, Vol. 77, p 751-759, 2000.

Timoshenko S., *Strength of Materials, Part II*, Van Nostrand Reinhold, 1958.

Wu H.Z., Huang Y.M., Adaptive simulation for tee-shape tube hydroforming processes, M. A. Sc. Thesis, Sun Yat-sen University, 2003 (in Chinese).

Yang H., Lin Y., Wrinkling analysis for forming limit of tube bending processes, Journal of Materials Processing Technology, Vol. 152, p 363-369, 2004.

Yao Y., A finite element analysis of the hydro-bulging of a toroidal shell, M.Eng. Thesis, University of Ottawa, 2005.

Zeng Y.S., Li Z.Q., Experimental research on the tube push-bending process, Journal of Materials Processing Technology, Vol. 122, p 237-240, 2002.

Zhang Y., Redekop D., Shell element simulation of the push method of tube bending, Journal of Achievements in Materials and Manufacturing Engineering, Vol. 17, p 301-304, 2006.

Publications Arising from This Research

Zhang Y., Redekop D., Shell element simulation of the push method of tube bending, Journal of Achievements in Materials and Manufacturing Engineering, Vol. 17, p 301-304, 2006.

Zhang Y., Redekop D., Experience in the explicit FEM simulation of the hydroforming of a tee-joint, Proc. CSME Forum, Calgary, p 1-7, 2006.

Zhang Y., Redekop D., Explicit FEM simulation of a new method of tube bending, Proc. ICAMEM Conference, Hammamet, Tunisia, p 1-6, 2006.

Zhang Y., Redekop D., FEM Simulation of the hydroforming of a y-joint, Fifth International Conference on Thin-Walled Structures, Brisbane, Australia, 2008, accepted.

Tables

Table 2.1 Model definition for T-joints

Case	D_1 (mm)	L (mm)	t (mm)	D_2 (mm)	H (mm)
1	76.2	300	3	76.2	60
2	76.2	300	5	76.2	60
3	76.2	300	3	50.8	60

Table 2.2 Properties of materials used in this thesis

Material	Young's modulus (GPa)	K (MPa)	n	Poisson's ratio
AA6063-T6 (Wu, 2003)	65.0	181.0	0.318	0.28
AA5052-O (Oyane, 1980)	70.0	401.0	0.300	0.30
SS304 (Jirathearantat, 2004)	200.0	1471.0	0.584	0.30

Table 3.1 Model definition for Y-joints

Model	D_0 (mm)	D_1 (mm)	t (mm)	Material	Tube length(mm)
1	50.8	50.8	0.89	AA6063-T6	500
2	50.8	50.8	1.25	AA6063-T6	500
3	50.8	50.8	1.65	AA6063-T6	500
4	50.8	44.5	1.25	AA6063-T6	500
5	50.8	50.8	0.89	SS304	500
6	50.8	50.8	1.25	SS304	500
7	50.8	50.8	1.50	AA5052-O	500

Table 3.2 Loading paths for different FEM models

Model	d_L (mm)	d_R (mm)	Internal pressure (MPa)
1	35.75	65.00	4.0
2	35.75	65.00	4.6
3	35.75	65.00	6.5
4	35.75	65.00	4.0
5	32.25	60.00	10.0
6	32.25	60.00	12.0
7	49.50	90.00	15.0

Table 3.3 Simulation results of model 1 for convergence

	Coarse mesh	Medium mesh	Refined mesh
Thick. change (thinning)	49.5%	50.2%	50.4%
Thick. change (thickening)	147.7%	141.2%	142.4%
Max. von Mises stress (MPa)	221.1	220.5	220.32
Max. plastic strain	0.82	0.84	0.84

Table 3.4 Simulation results for parametric study

Model	Final thickness		Max. von Mises stress (MPa)	Max. plastic strain
	Thinning	Thickening		
1	50.4%	142.4%	220.32	0.84
2	52.1%	133.3%	216.18	0.85
3	56.7%	123.8%	219.04	0.87
4	58.4%	130.6%	160.45	0.81
5	60.2%	125.5%	1454.00	0.82
6	63.9%	121.6%	1576.54	0.82
7	44.7%	135.3%	299.78	0.90

Table 3.5 Model definition for angle parametric study

Model	D_0 (mm)	D_1(mm)	t (mm)	Material	Angle (degree)
2	50.8	50.8	1.25	AA6063-T6	60
8	50.8	50.8	1.25	AA6063-T6	75
9	50.8	50.8	1.25	AA6063-T6	90

Table 3.6 Loading paths for angle parametric models

Model	d_L (mm)	d_R (mm)	Internal pressure (MPa)
2	35.75	65.00	4.0
8	45.50	65.00	4.0
9	65.00	65.00	4.0

Table 3.7 Simulation results for angle parametric study

Model	Final thickness		Max. von Mises stress (MPa)
	Thinning	Thickening	
2	55.5%	119.2%	163.90
8	69.3%	124.0%	163.73
9	73.9%	130.0%	168.47

Table 4.1 Validation for spring-back:

comparison with experimental results for aluminum alloys

Material	5052-O	2024-O	5052-O	5052-O
r_1 (mm)	6.35	19.15	12.70	3.18
r_2 (mm)	5.33	17.45	11.00	2.29
σ_0 (MPa)	99.96	109.76	99.96	99.96
E (MPa)	70.0×10^3	72.0×10^3	70.0×10^3	70.0×10^3
ρ_0 (mm)	40.00	152.40	76.20	25.00
ρ_0/ρ_f (Al-Qureshi 2002)	0.982	0.965	0.990	0.969
ρ_0/ρ_f (theory)	0.988	0.984	0.989	0.984
Error (%)	0.61	1.97	0.10	1.55

Table 4.2 Validation and parametric models for tube push-bending

Model	OD (mm)	Bending radius (ratio of OD)	Tube thickness (mm)
V1	40.00	1.75	1.20
A11	41.27	1.00	0.89
A12			1.25
A13			1.65
A21		1.50	0.89
A22			1.25
A23			1.65
A31		2.00	0.89
A32			1.25
A33			1.65
B11	50.80	1.00	0.89
B12			1.25
B13			1.65
B21		1.50	0.89
B22			1.25
B23			1.65
B31		2.00	0.89
B32			1.25
B33			1.65

Table 4.3 Convergence of results for model V1

Mesh density	Coarse mesh	Medium mesh	Refined mesh
Thickness at extrados (mm)	1.74	1.71	1.72
Thickness at intrados (mm)	1.18	1.15	1.13
Max. von Mises stress at extrados (MPa)	138.76	150.31	150.55
Max. von Mises stress at intrados (MPa)	218.20	215.60	220.00

Table 4.4 Comparison of current results for wall thickness with previous results (model V1 with aluminum alloy material)

Cross section	Previous results (Baudin *et al*, 2004) (mm)		Current results (mm)	
	Extrados	Intrados	Extrados	Intrados
A	1.34	1.63	1.34	1.58
B	1.05	1.51	1.14	1.50
C	1.22	1.24	1.19	1.32

Table 4.5 Simulation results for wall thickness and maximum von Mises stress

Model	Thickness (mm)		Max. von Mises stress (MPa)	
	Extrados	Intrados	Extrados	Intrados
A11	0.94	1.45	139.2	232.0
A12	1.24	1.91	143.2	225.4
A13	1.62	2.56	146.6	220.7
A21	0.86	1.27	144.8	214.8
A22	1.19	1.70	147.4	203.0
A23	1.54	2.25	151.8	202.4
A31	0.87	1.20	141.1	177.3
A32	1.20	1.65	145.2	178.3
A33	1.56	2.14	149.7	178.7
B11	0.73	1.21	164.3	195.2
B12	1.06	1.75	167.1	197.5
B13	1.39	2.24	171.1	197.9
B21	0.75	1.16	146.6	154.7
B22	1.09	1.65	146.4	157.9
B23	1.42	2.21	147.2	154.8
B31	0.76	1.11	145.9	146.4
B32	1.10	1.58	144.9	150.9
B33	1.48	2.09	143.2	150.4

Table 4.6 Simulation results for the spring-back, material waste, and maximum axial load

Model	Spring-back factor		Material waste (mm)	Maximum axial load (10kN)
	Theory	FEM		
A11	0.995	0.965	24.7	3.67
A12	0.994	0.967	21.1	4.01
A13	0.994	0.970	22.8	4.46
A21	0.992	0.974	21.9	3.44
A22	0.992	0.971	22.3	3.84
A23	0.992	0.975	23.4	4.31
A31	0.989	0.965	19.6	2.52
A32	0.989	0.966	17.8	2.93
A33	0.989	0.960	16.5	3.21
B11	0.995	0.975	32.4	4.44
B12	0.995	0.976	32.4	4.86
B13	0.995	0.980	30.5	5.73
B21	0.992	0.972	28.6	5.17
B22	0.992	0.974	28.2	5.73
B23	0.992	0.977	27.4	6.35
B31	0.989	0.963	28.1	5.02
B32	0.989	0.960	26.9	5.91
B33	0.989	0.966	26.1	6.23

Table 4.7 Simulation results for steel tube (model V1)

Cross section	Thickness (mm)		Max. von Mises stress (MPa)	
	Extrados	Intrados	Extrados	Intrados
A	1.36	1.90	130	330
B	1.07	1.56	170	250
C	1.25	1.23	120	130

Table 4.8 Simulation results for friction coefficient of 0.15

(model V1 with AA6063-T6)

Cross section	Thickness (mm)		Max. von Mises stress (MPa)	
	Extrados	Intrados	Extrados	Intrados
A	1.33	1.54	140	50
B	1.10	1.48	100	150
C	1.19	1.31	70	120

Figures

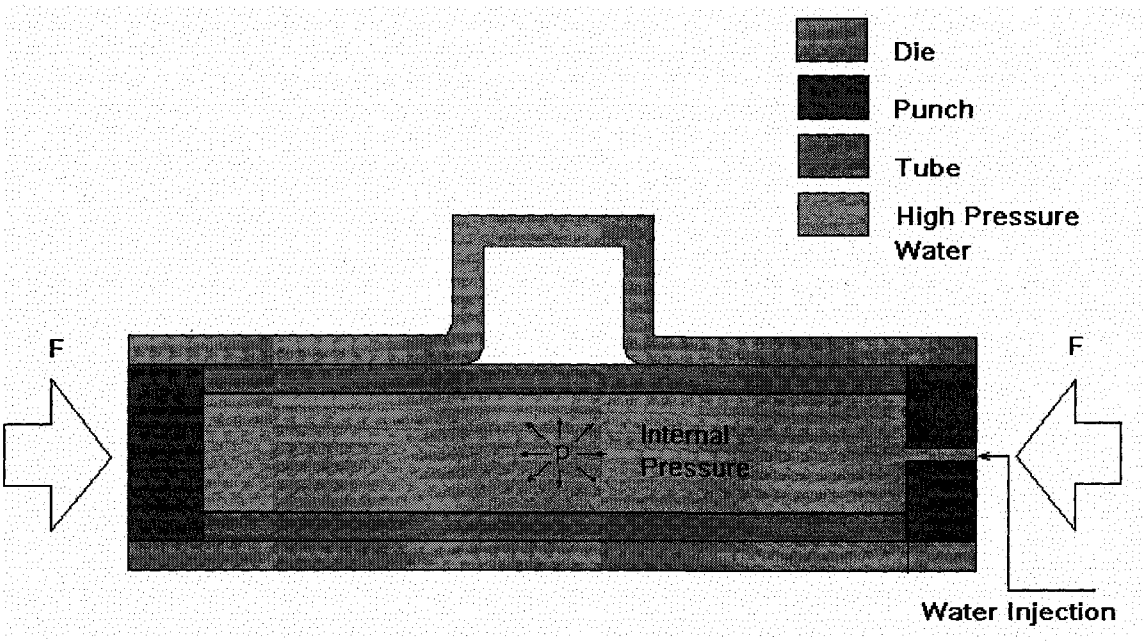

Fig. 1.1 Illustration of tube hydroforming for a T-joint

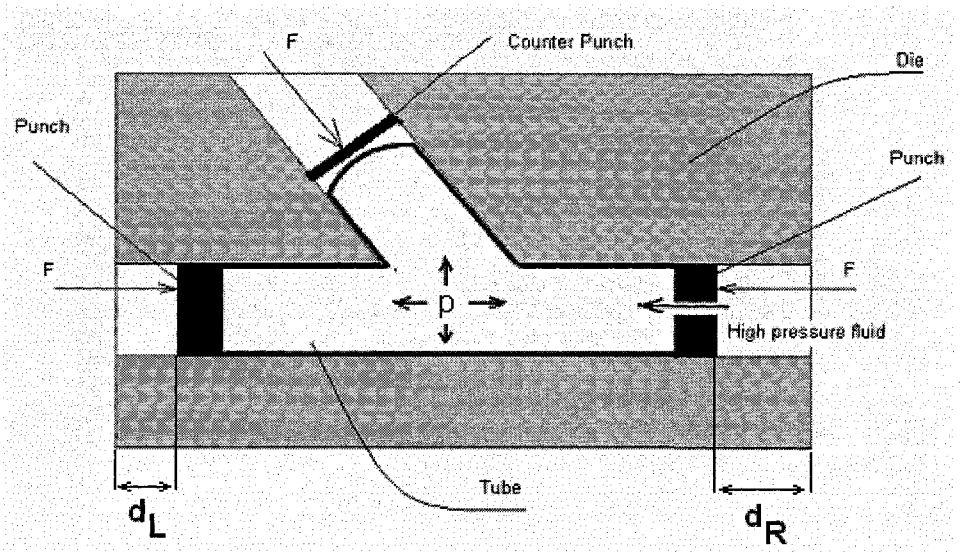

Fig. 1.2 Illustration of Y-hydroforming

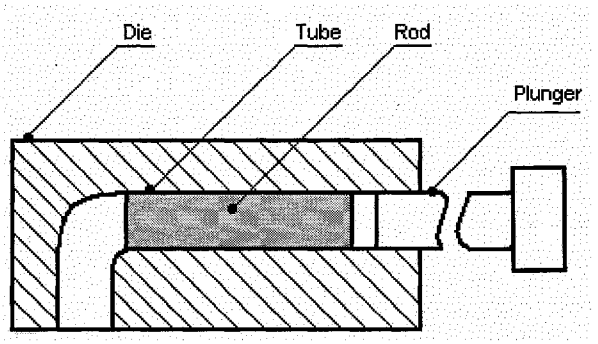

Fig. 1.3 Symbolic representation of tube push-bending (before forming)

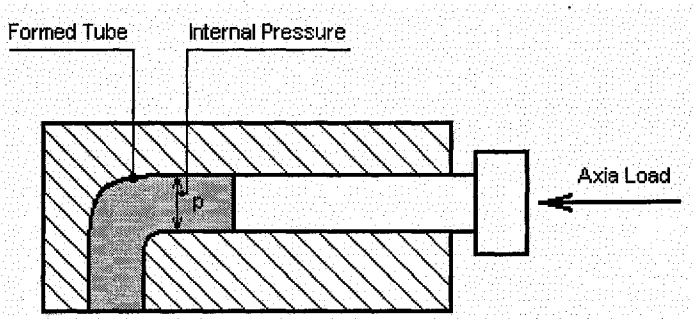

Fig. 1.4 Symbolic representation of tube push-bending (after forming)

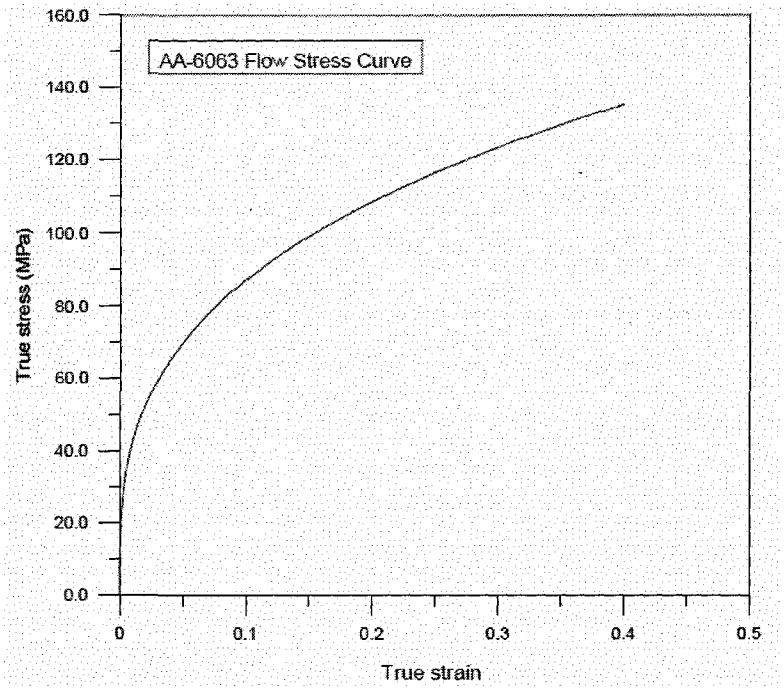

Fig. 1.5 Strain-stress curve for AA6063 (Wu, 2003)

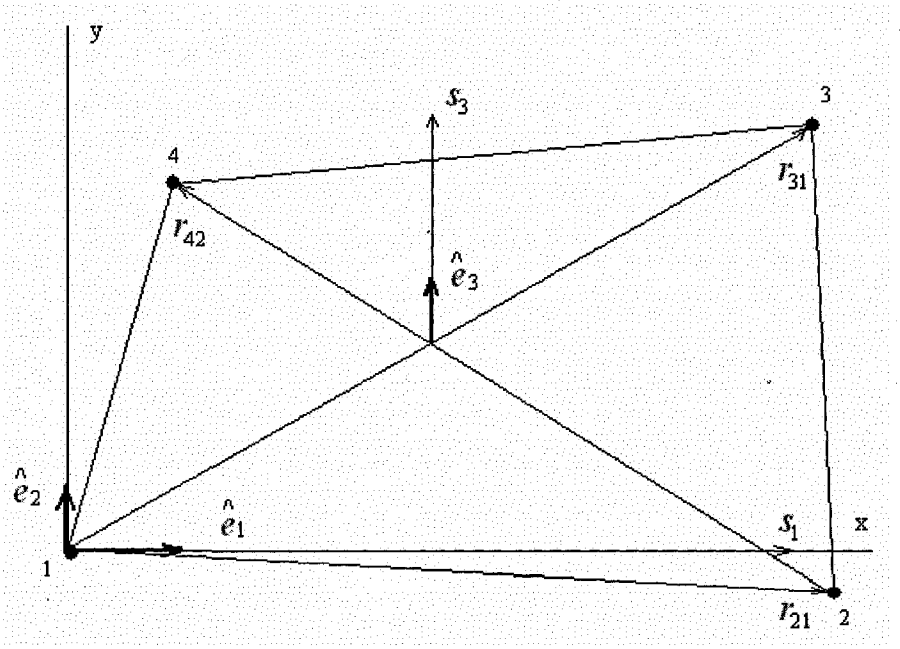

Fig. 1.6 Construction of element coordinates system

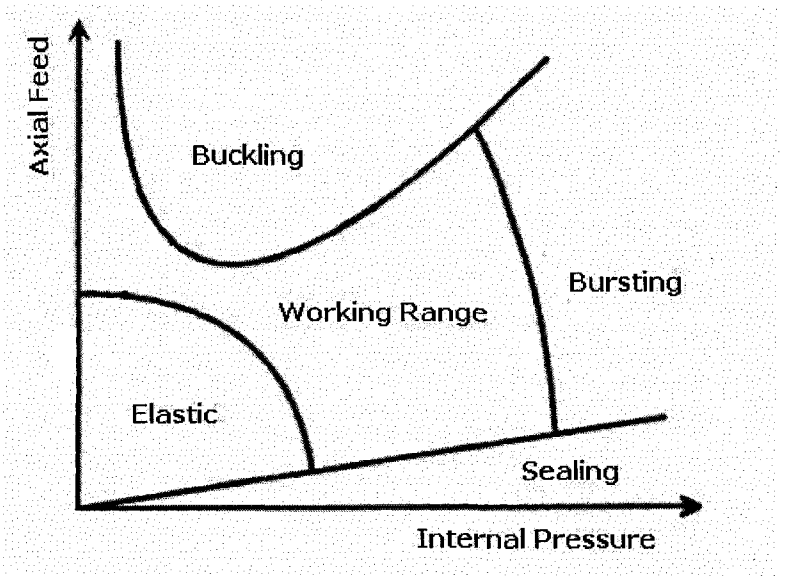

Fig. 2.1 Symbolic interaction diagram of working range (Wu, 2003)

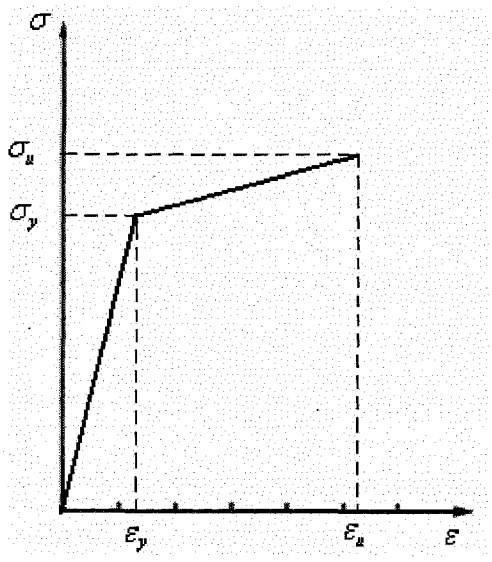

Fig. 2.2 Bilinear elastic-plastic material stress-strain relation

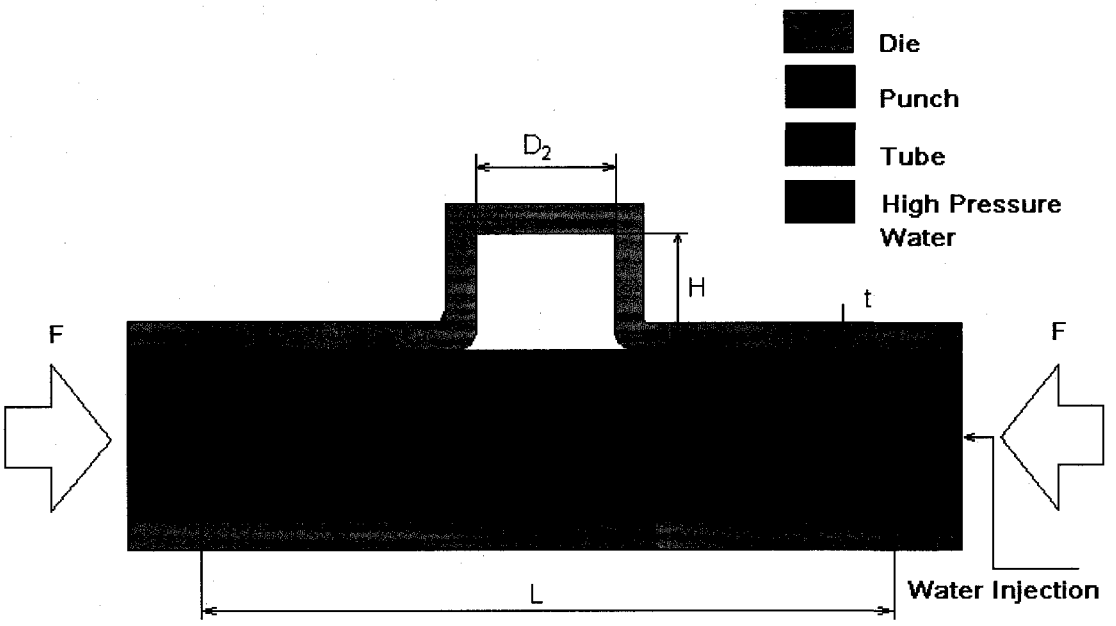

Fig. 2.3 Geometry for T- hydroforming

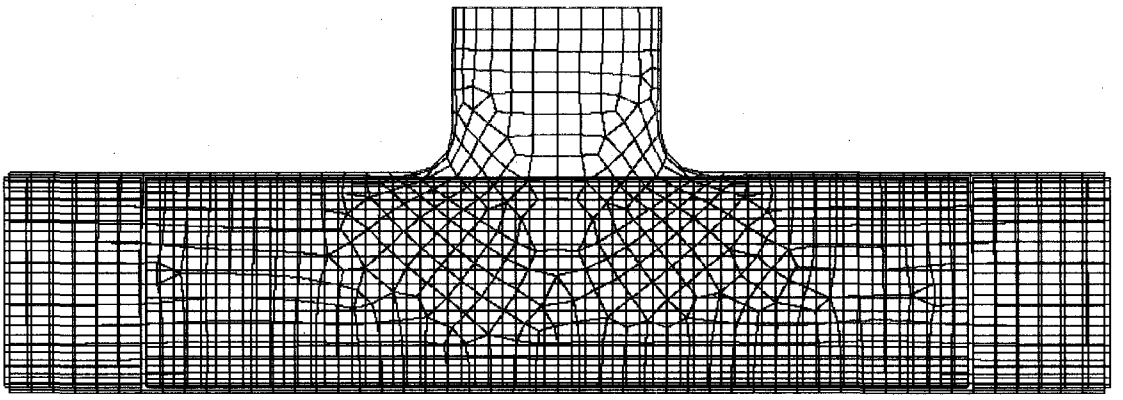

Fig. 2.4 FEM mesh of die and blank

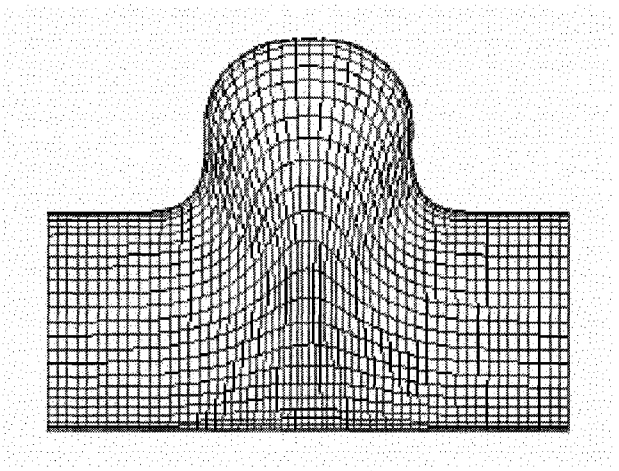

Fig. 2.5 Satisfactory forming with deformed mesh

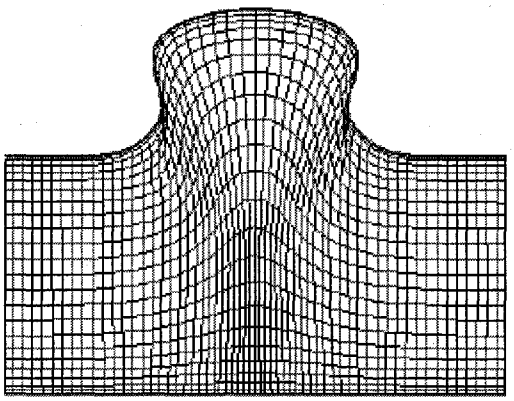

Fig. 2.6 Product with fillet area defect

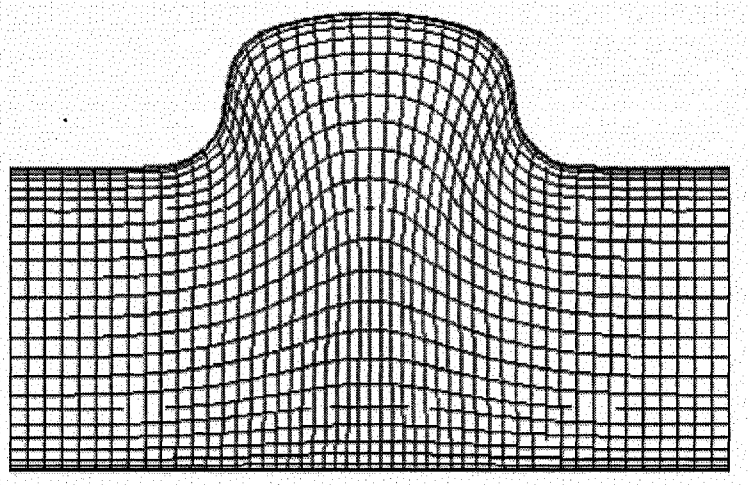

Fig. 2.7 Product with incomplete forming

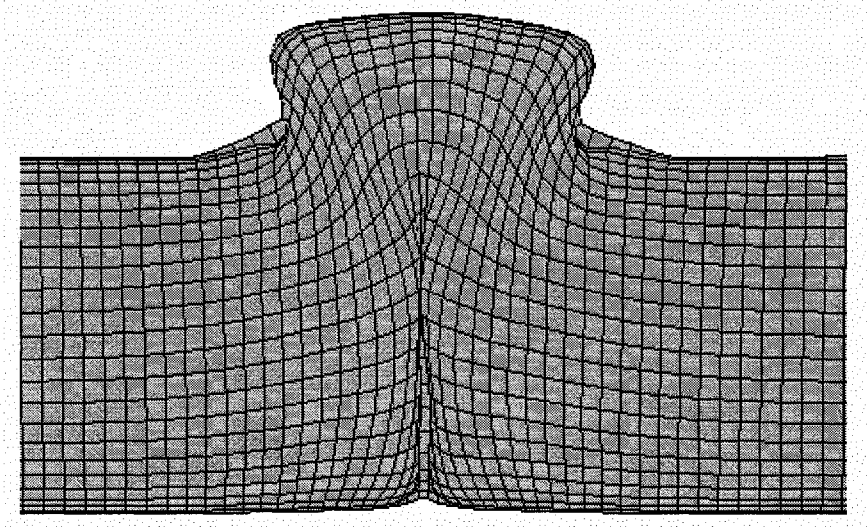

Fig. 2.8 Product with buckling

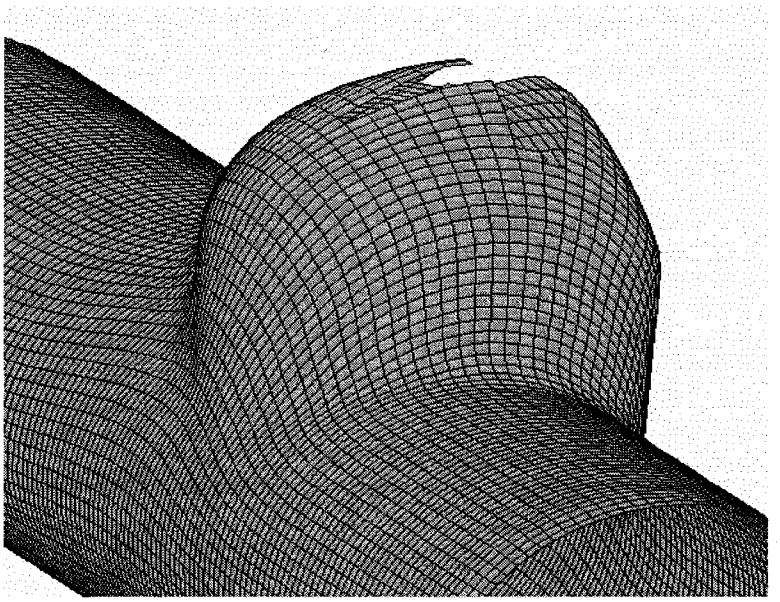

Fig. 2.9 Product with bursting

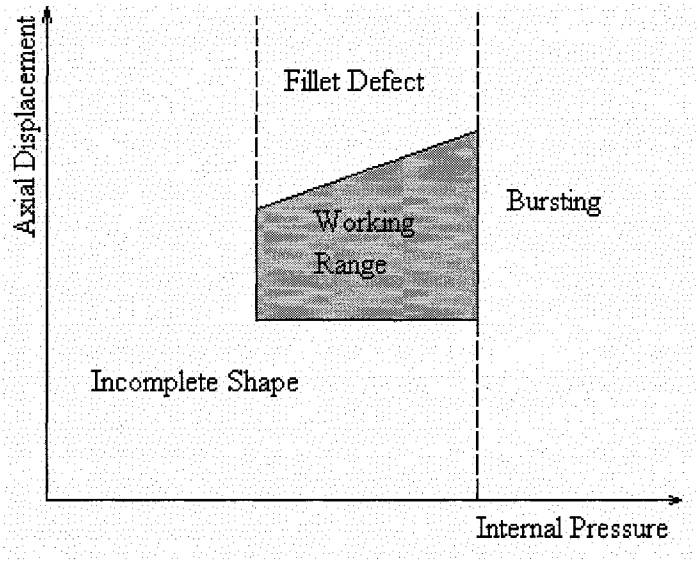

Fig. 2.10 Modified working range diagram for displacement-controlled loading

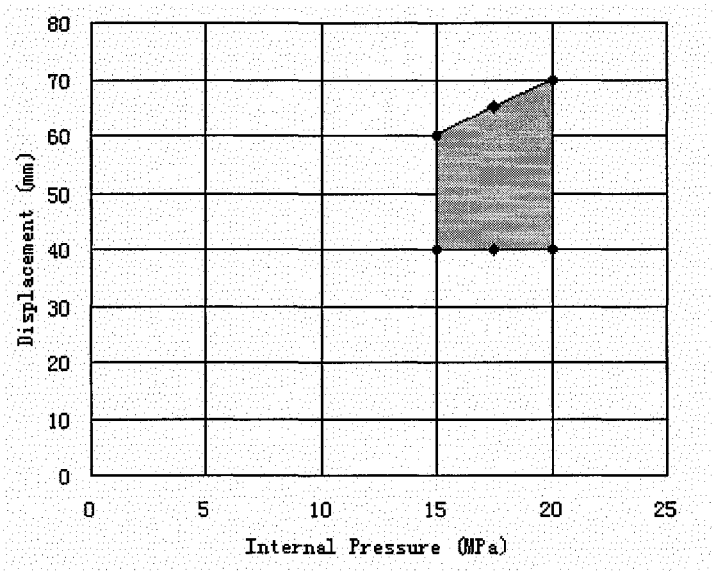

Fig. 2.11 Working range for case 1

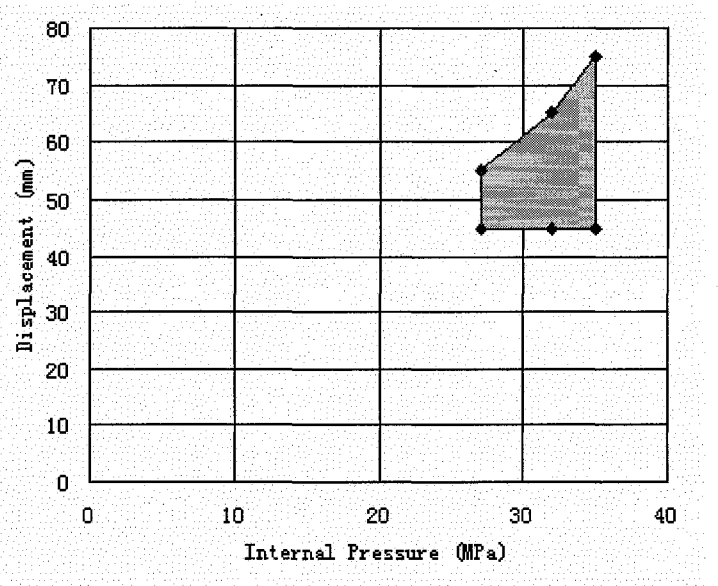

Fig. 2.12 Working range for case 2

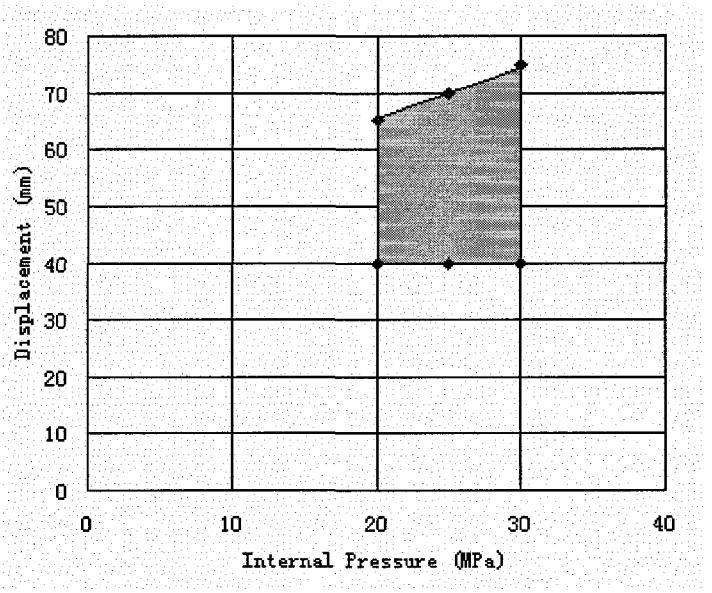

Fig. 2.13 Working range for case 3

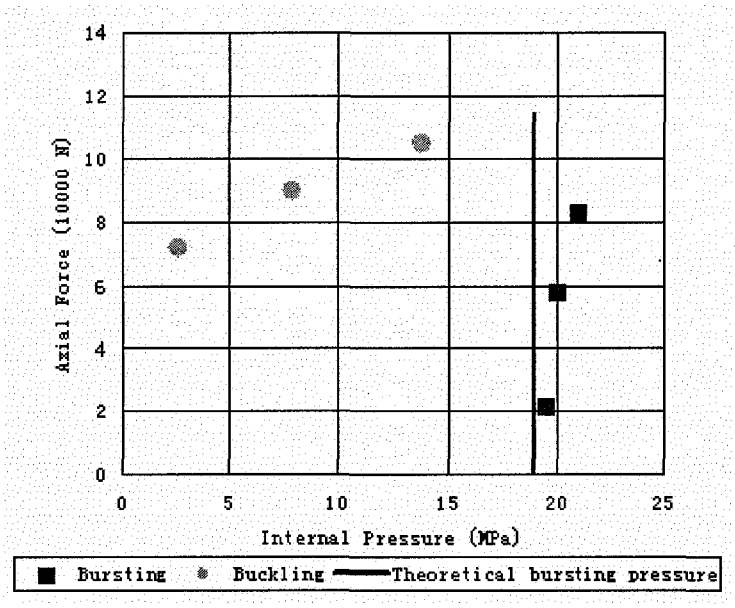

Fig. 2.14 Bursting and buckling for case 1

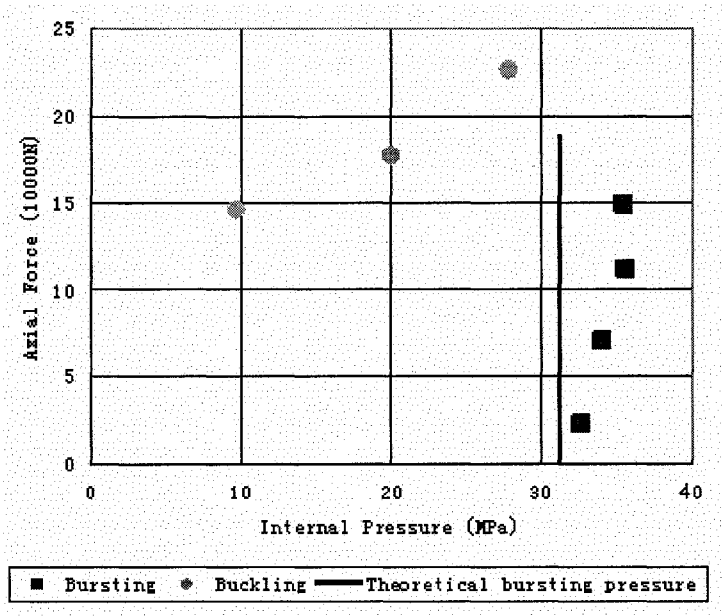

Fig. 2.15 Bursting and buckling for case 2

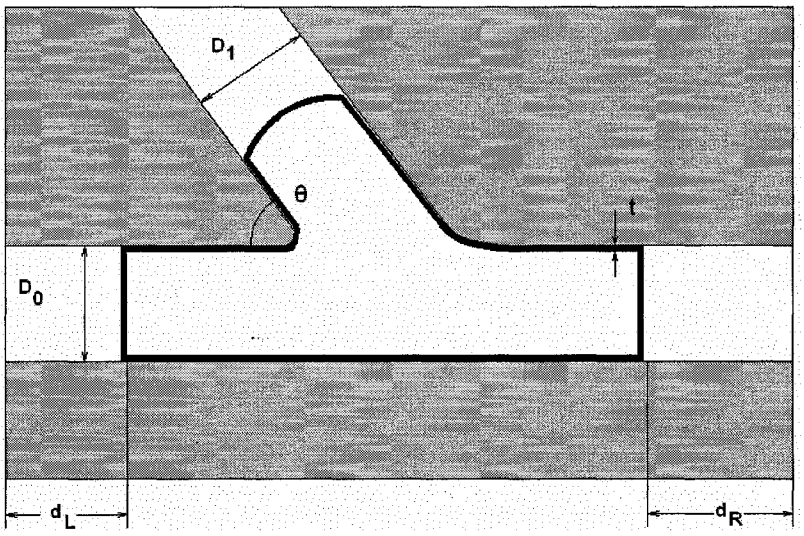

Fig. 3.1 Geometry and axial loading feeds for Y-hydroforming

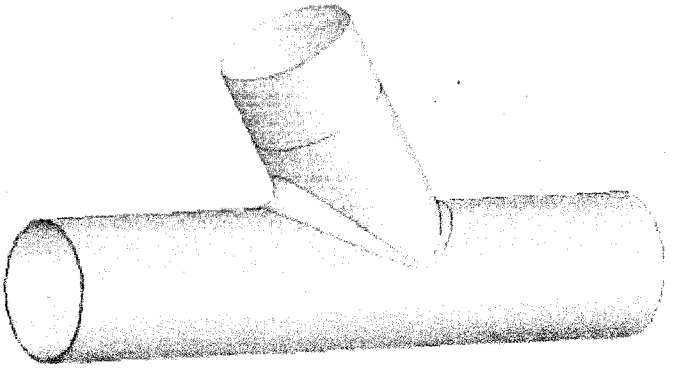

Fig. 3.2 Model from SolidWorks

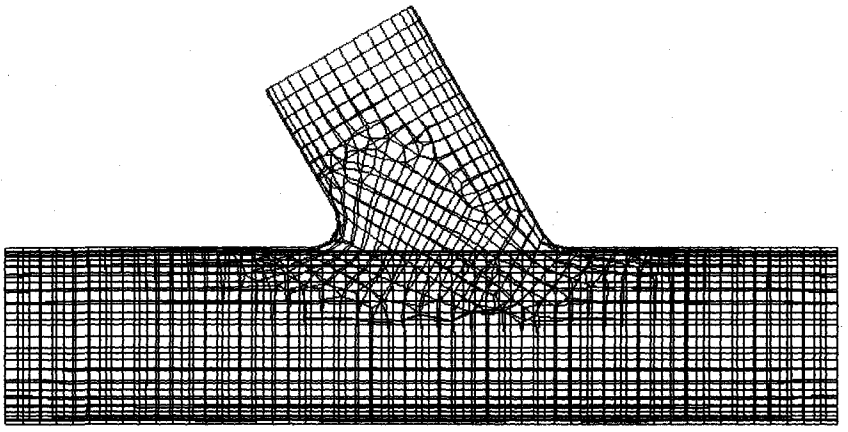

Fig. 3.3 FEM mesh for die and tube blank

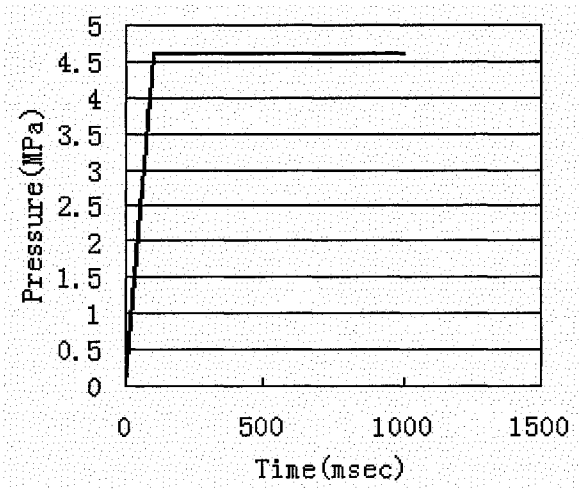

Fig. 3.4 Internal pressure vs. time (Model 2)

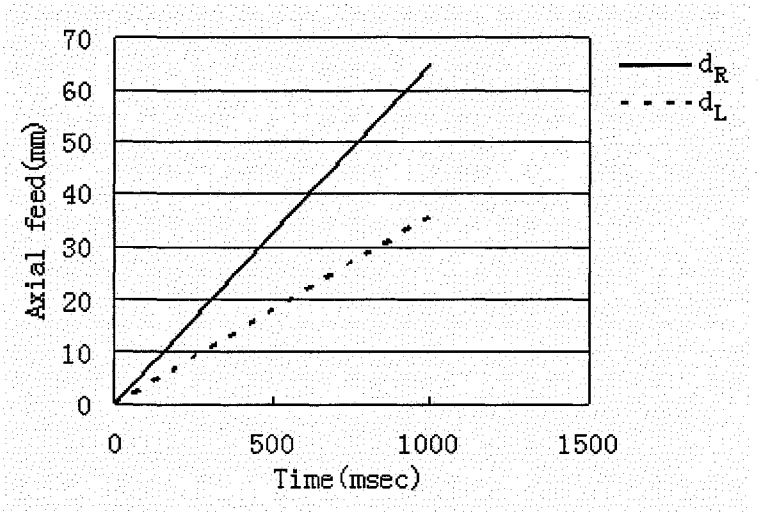

Fig. 3.5 Axial feeds for punches d_R and d_L vs. time (Model 2)

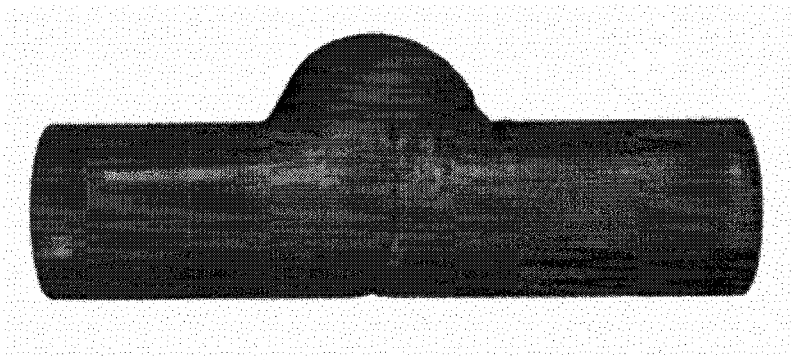

Fig. 3.6 Buckling in FEM simulation

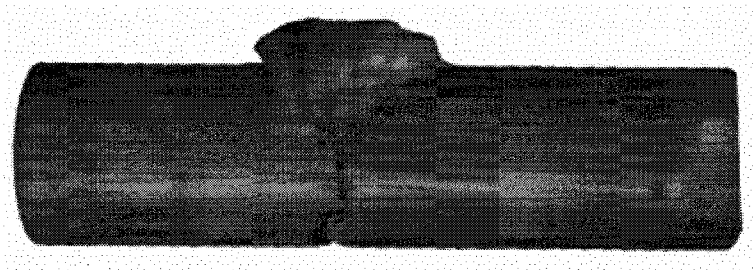

Fig. 3.7 Incomplete protrusion and buckling in FEM simulation

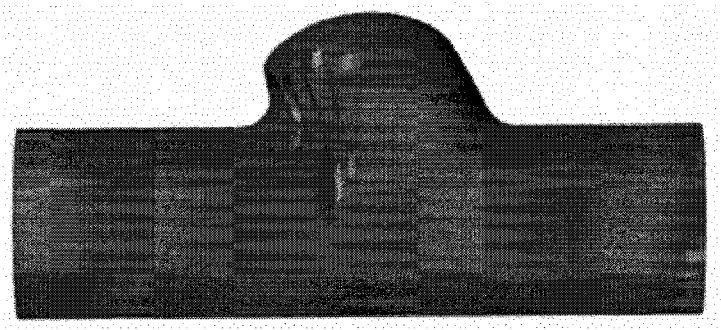

Fig. 3.8 Fillet defect in FEM simulation

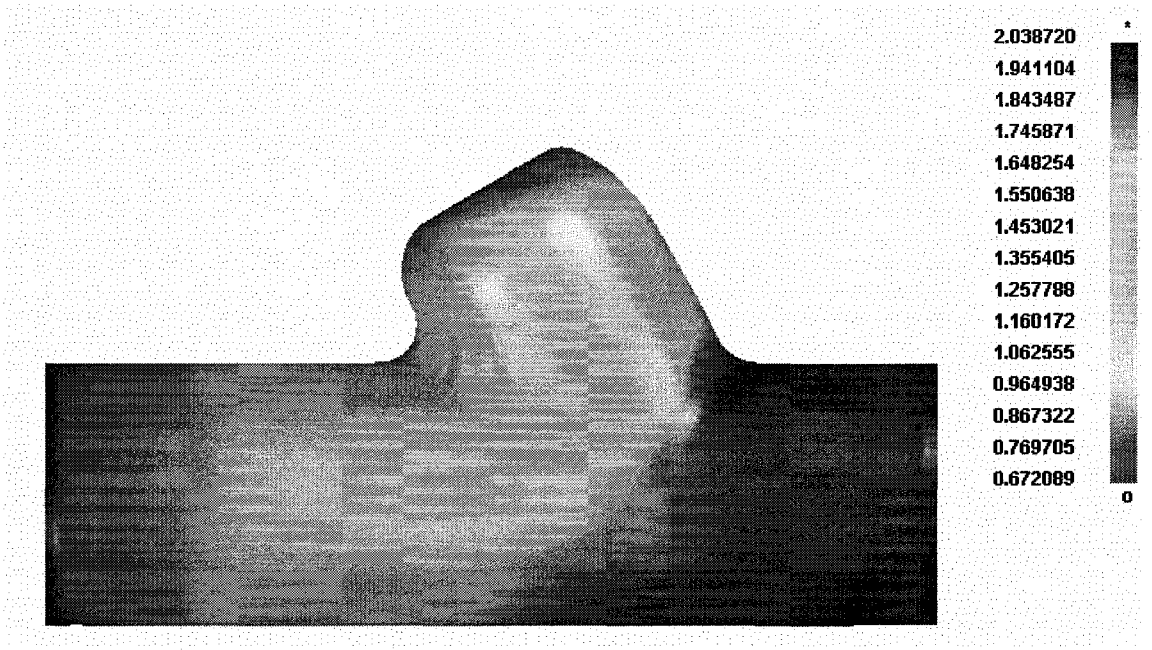

Fig. 3.9 Contour of thickness distribution of model 7 (in mm)

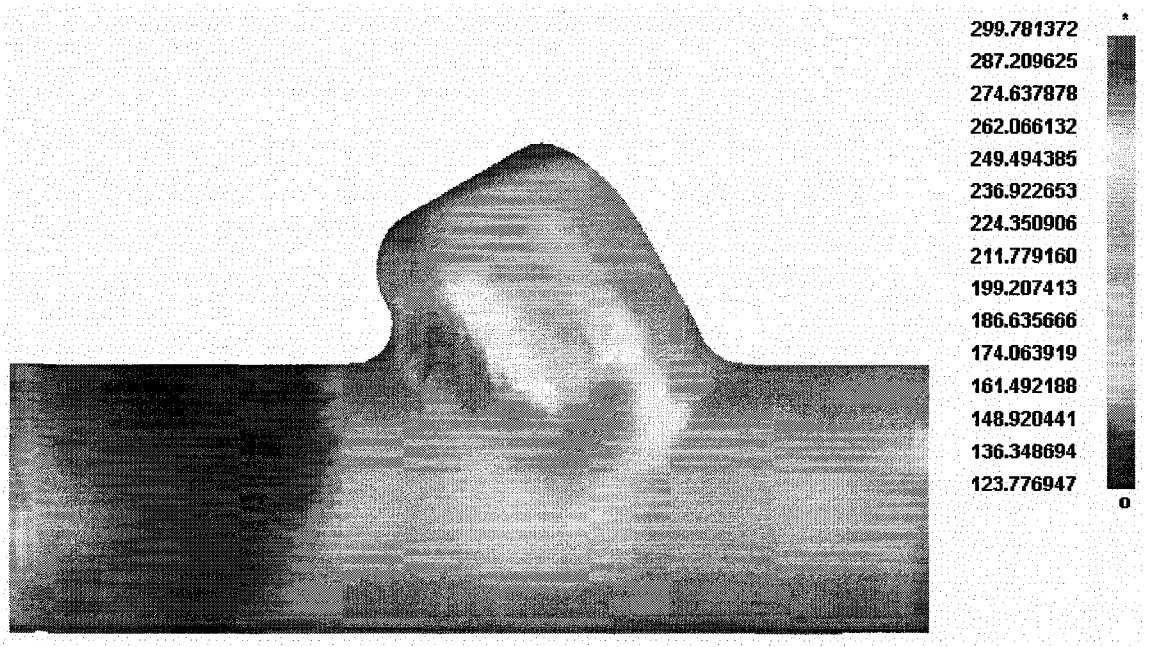

Fig. 3.10 Contour of maximum von Mises stress distribution of model 7 (in MPa)

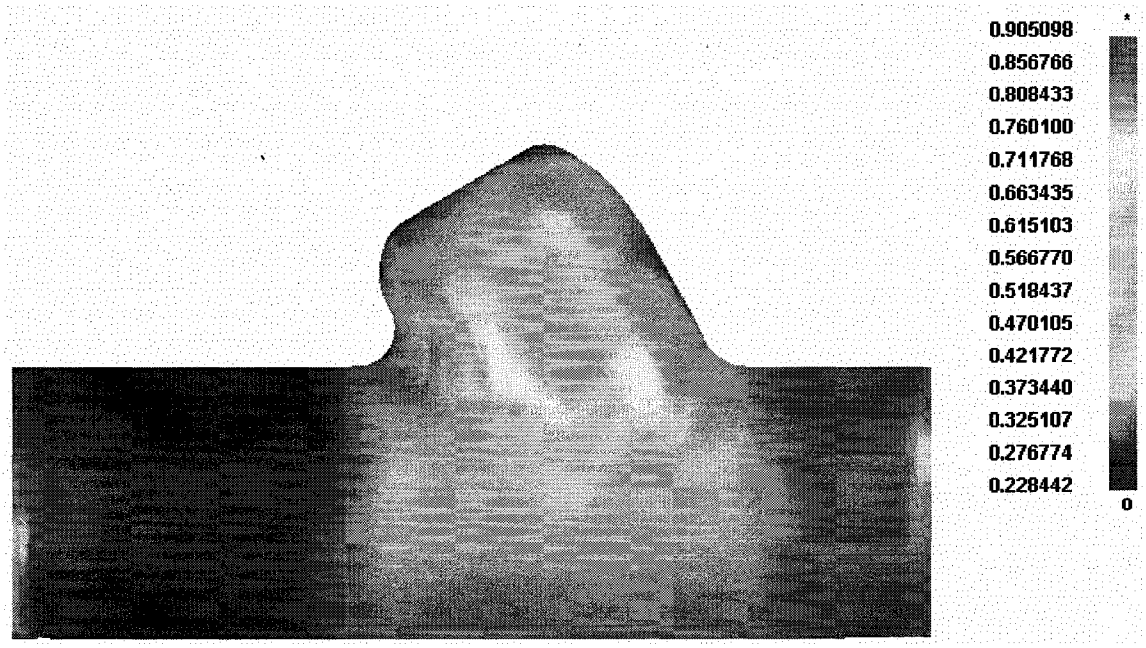

Fig. 3.11 Contour of plastic strain distribution of model 7 (dimensionless)

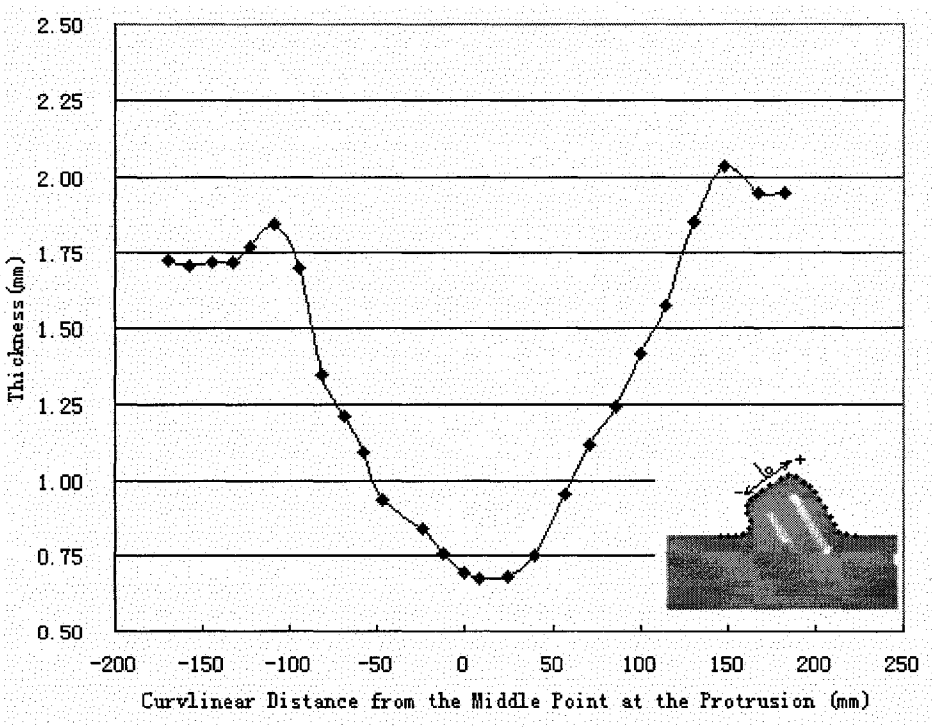

Fig. 3.12 Thickness distribution at longitudinal section of model 7

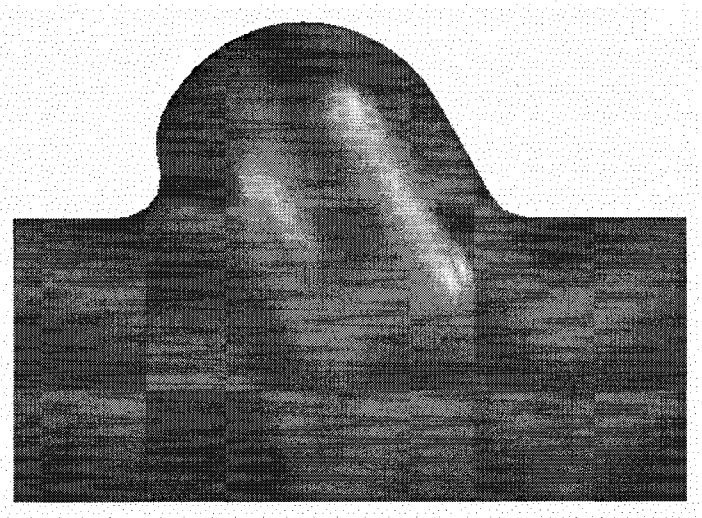

Fig. 3.13 Simulation result for Y-angle θ=60°

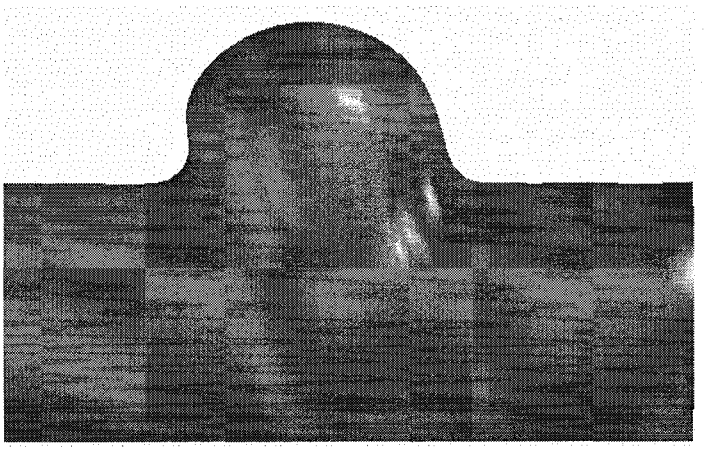

Fig. 3.14 Simulation result for Y-angle θ=75°

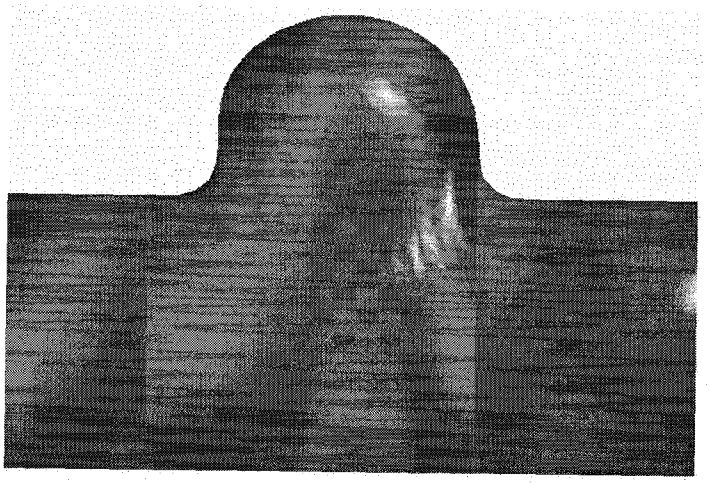

Fig. 3.15 Simulation result for Y-angle θ=90° (i.e. tee)

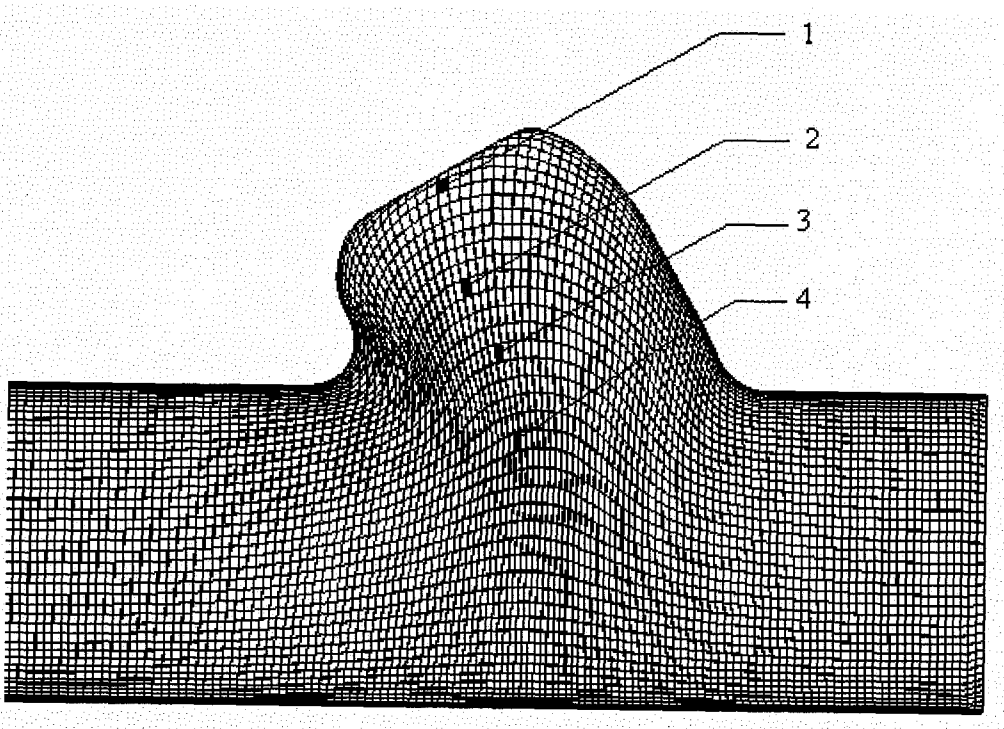

Fig. 3.16 Selection of four shell elements for bursting prediction

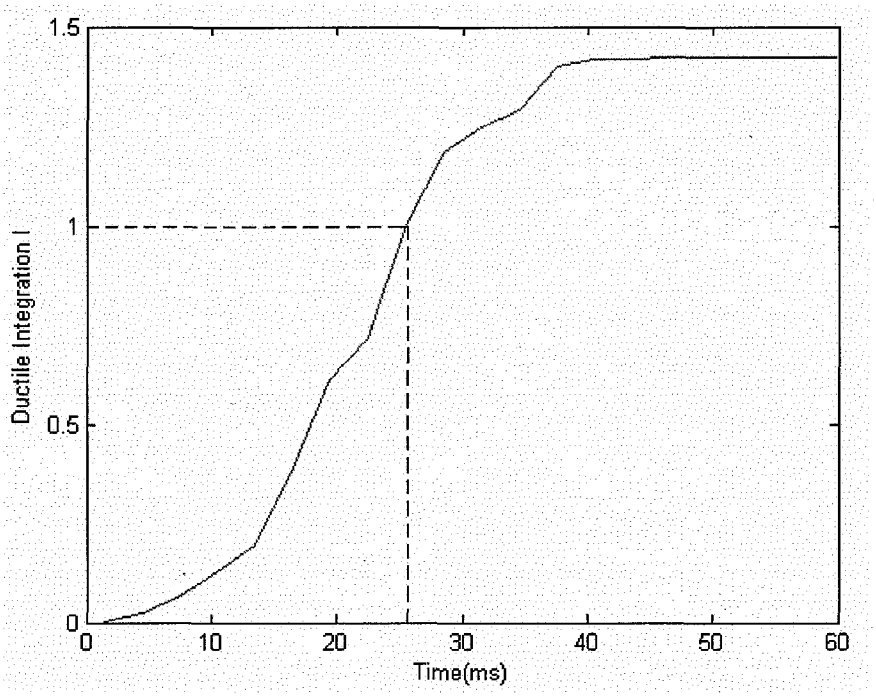

Fig. 3.17 Plot of the ductile fracture integral I with time

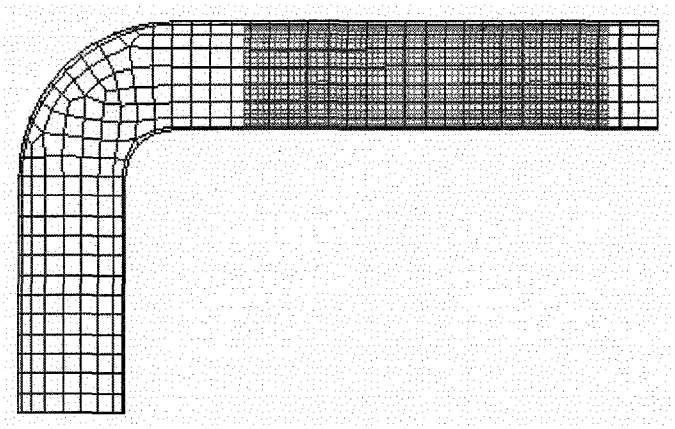

Fig. 4.1 FEM model of die and blank - before forming

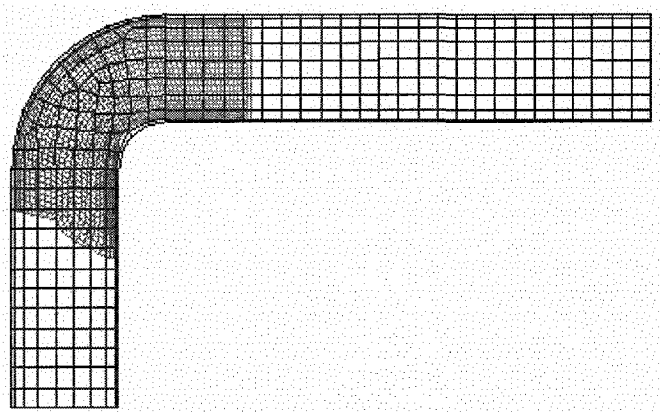

Fig. 4.2 FEM mesh of die and blank - after forming

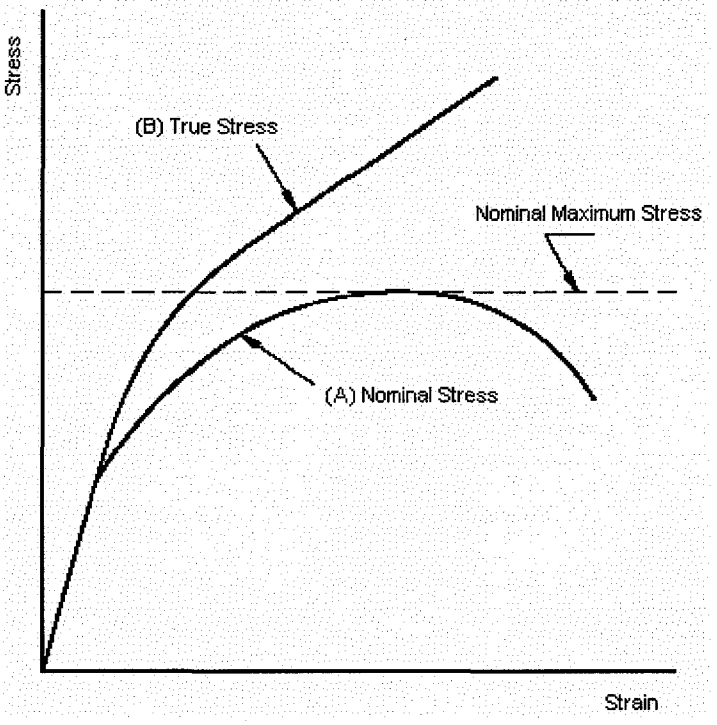

Fig. 4.3 Nominal stress-strain curve versus the true stress-strain curve

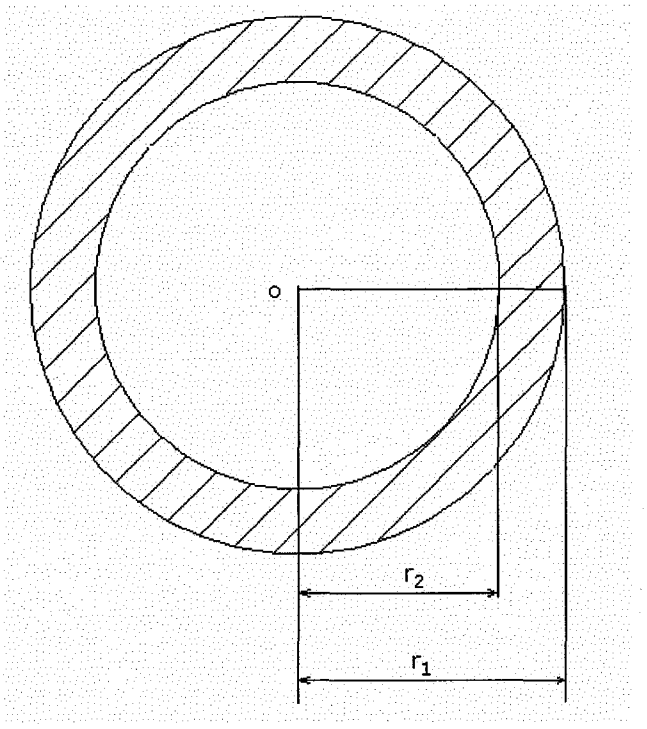

Fig. 4.4 Geometry for the cross-section of the tube

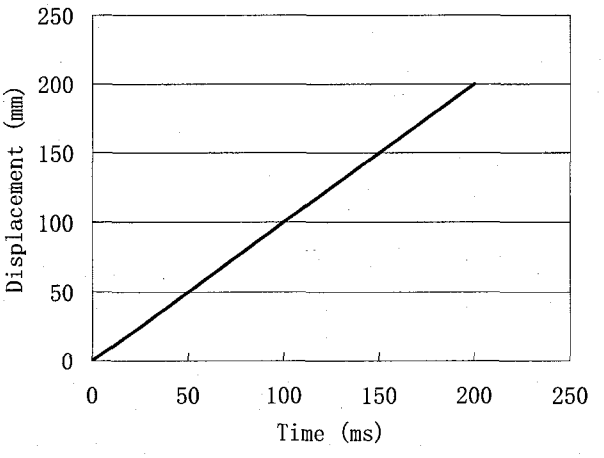

Fig. 4.5 Axial feeds vs. time (Model V)

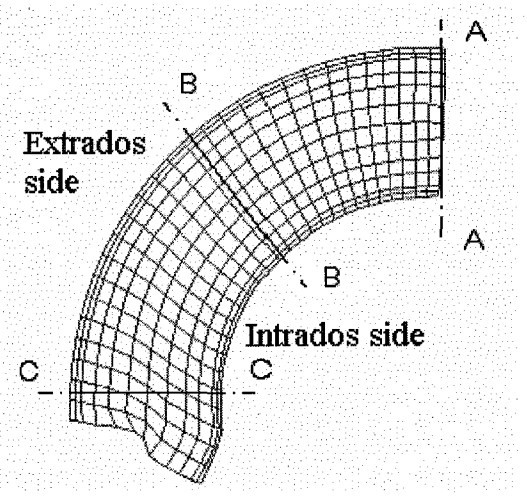

Fig. 4.6 Positions of cross-sections A, B, and C for Tables 4.4, 4.7, 4.8

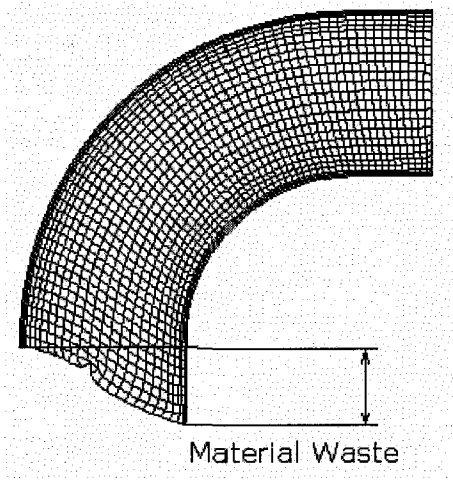

Fig. 4.7 Illustration of material waste

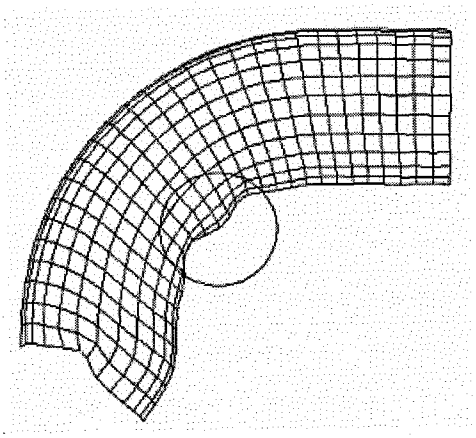

Fig. 4.8 (a) Forming results, with wrinkling

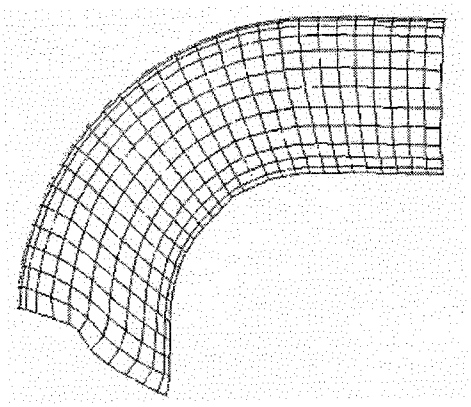

Fig. 4.8 (b) Forming results, without wrinkling

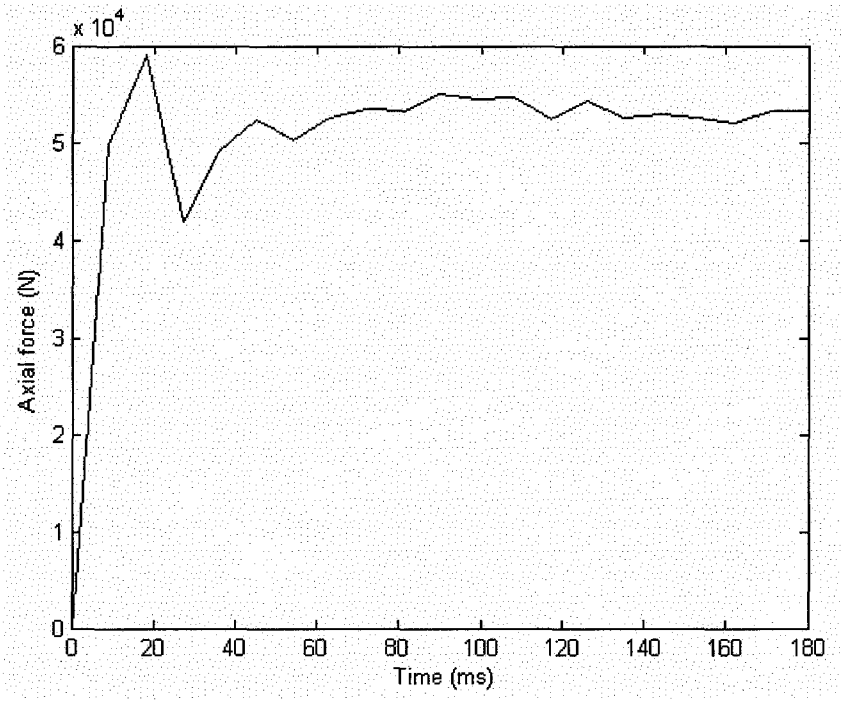

Fig. 4.9 Plot of axial force on cross-section of tube's end versus time

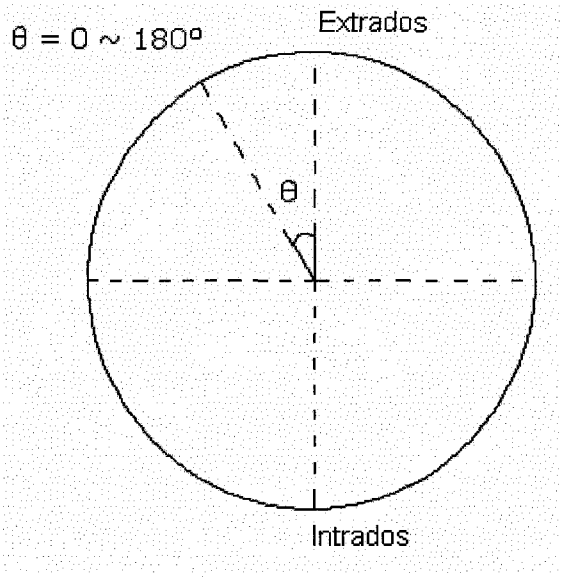

Fig. 4.10 Definition of the cross-section angle θ for stress distribution description

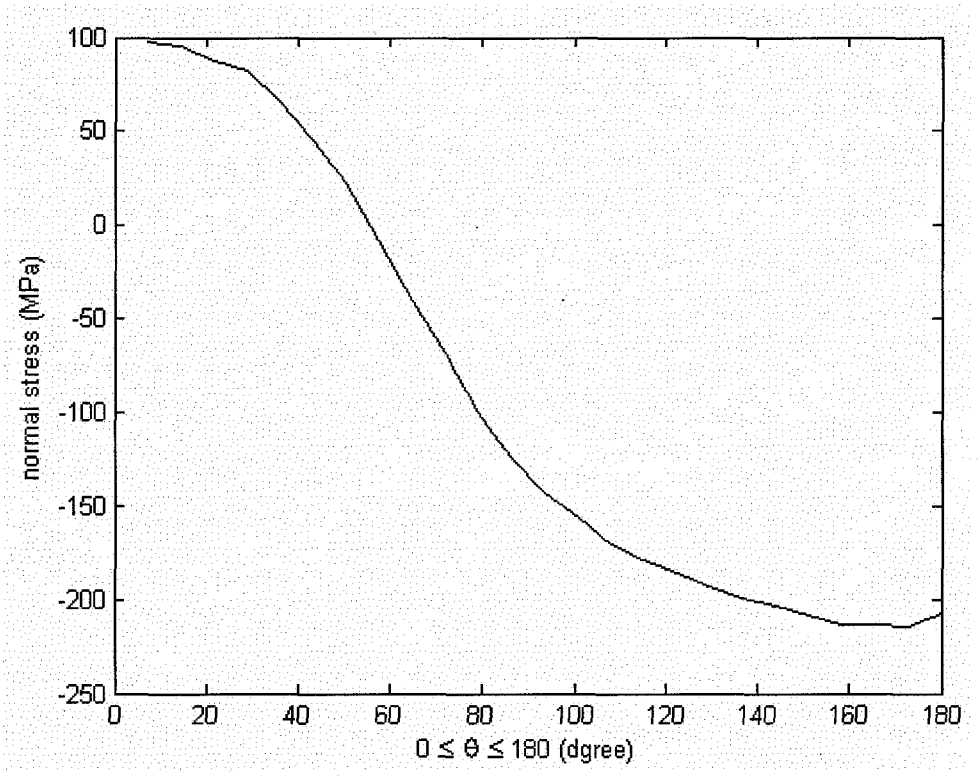

Fig. 4.11 Axial normal stress versus cross-section angle θ for model A33

Appendix A: Software Instructions

These instructions introduce the procedure of simulating the T-hydroforming. Models for this simulation were generated by Solidworks and were imported into pre-processor FEMB.

I Building the FEM model

The geometric model of the die was built in SolidWorks. The reason of building the die part in SolidWorks is that it is difficult to describe the fillet area in FEMB. The model then can be imported by the pre-processor FEMB. The imported model is treated as several surfaces and lines. We need to mesh those surfaces and apply all boundary conditions to the model.

First, import models from SolidWorks using Pre-Processor FEMB 28.0

Run FEMB 28.0.

Import the die model from an IGES file.

File->import-><modelname>.igs->open.

Click "Element" menu, then click "PLATE/SOLID MESH" button.

Click "TOPOLOGY MESH" button on the coming menu.

Click "Current Part", then click "APPLY".

Define a element size in the coming dialogue window. Then click "OK".

The model will be automatically meshed by the software.

The meshed model of the die is shown in Fig A-1.

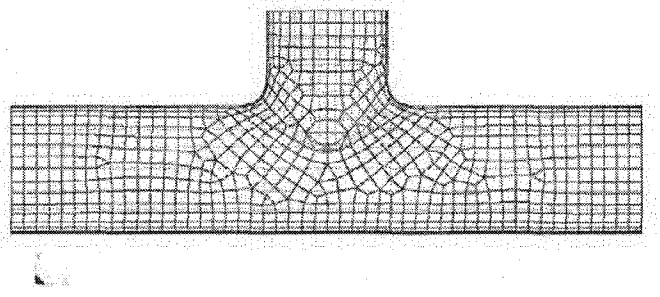

Fig. A-1

Build the tube's model

Part->Great Part->Tube->OK

Line->create->arc->about a centre->define->key-in-> 40, 0, 0 -> 40, 10, 0->40, 0, 10

Fill 38.1, 0, 180, 5 in the following message.

Here we have a half circle.

Line->Copy Line->Translate

Pick the line we just drew.

Translate->Global

Enter 300,0,0,1 in the following message box. Press Yes when is asked if the new line is in the original part.

Line->Create->Line(s).

Connect the four end points of the two separate lines.

Surface->Create->4 lines surface

Select the four lines as a clockwise (or anti-clockwise) order.

The tube's surface is modeled by now as Fig. A-2 shows.

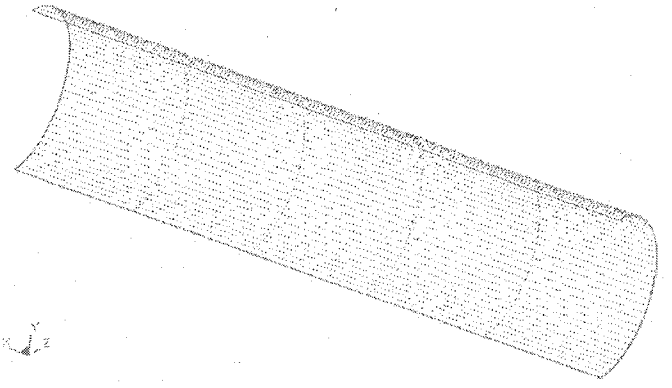

Fig. A-2

To build the punch's model, we need to create a new part.

Take the right punch for example, the left one can be simply copied from the right one.

Part->Great Part->Right Punch->OK

Line->create->arc->about a centre->define->key-in-> 38, 0, 0 -> 38, 10, 0 ->38, 0, 10

Fill 40, 0, 180, 5 in the following message.

Here we get a half circle.

Line->Copy Line->Translate

Pick the line we just drew.

Translate->Global

Enter -40, 0, 0, 1 in the following message box. Press Yes when is asked if the new line is in the original part.

Connect the two lines following the way in step 2

Connect the two end point of each line.

Now there are 6 lines in this part.

For the punch consisted by 4 surface (2 2-line surfaces 2 4-line surface), we have to create these surface.

From Fig. A-3, we could notice there are 6 lines

Surface->create->4-line surface

Pick 1, 2, 3, 4 -> OK

Surface->create->4-line surface

Pick 3, 5, 1, 6 -> OK

Surface->create->2-line surface

Pick 2, 5 -> OK

Surface->create->4-line surface

Pick 4, 6 -> OK

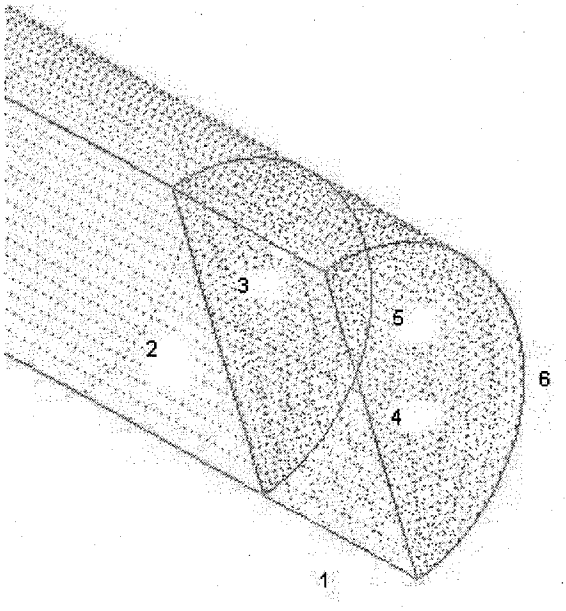

Fig. A-3

To see the full model, we need to open all part; make them visiable

The full model is shown in Fig. A-4.

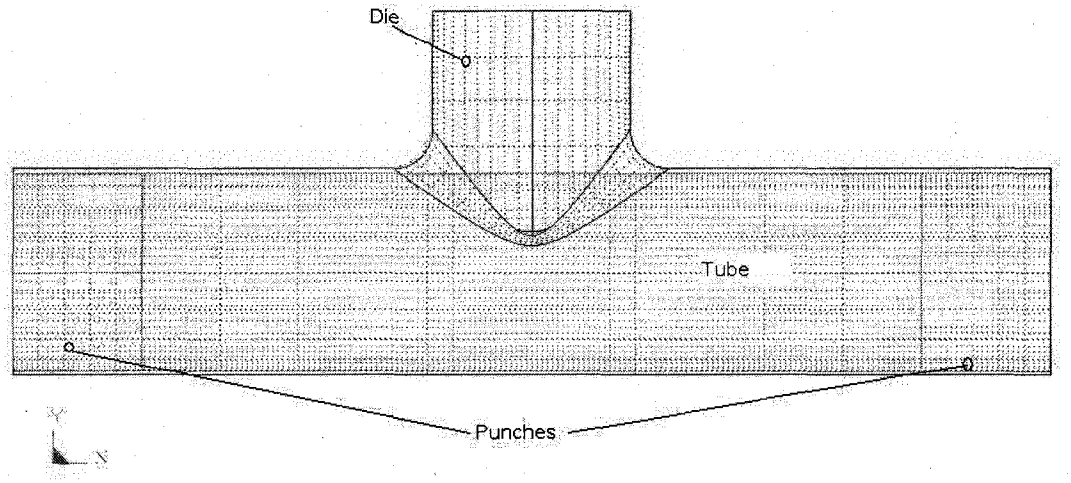

Fig. A-4

The punches and the tube are also need to be meshed:

Element->Plate-Solid Mesh->Topology Mesh->By Parts

Select the two punches parts from list on the left.

Apply->Apply

Enter 8 in the element size blank of the following message box.

OK->YES->YES

Repeat these steps to mesh tube part; the element size is 5 for tube part.

Material Defining:

Material->Create->Structural...->*18.1 Mat_Power_Law_Plastisity

RO: 2.67

E: 6.5e+04

PR: 2.8e-01

K: 1.81e+02

N: 2.18e-01

OK

Material->Create->Structural...->*20.1 Mat_Rigid

RO: 7.83

E: 2.0e+05

PR: 2.0e-01

OK

Material->Assign->1. M-1->2 Tube->Apply

Material->Assign->1. M-2->1 Die; 3 Punch 1; 4 Punch 2->Apply

Property

Property->Create->Shells

Select the item No. 1.1 in the left window.

Fill following values in the right window:

ELFORM: 2

SHRF: 1.0

NIP: 2

PROPT 0

QR/IRID: 0

ICOMP: 0

SETYP: 1

Select the item No. 2.1 in the left window.

Fill following values in the right window:

T1~T4 : 3.0

Property->Create->Shells

Select the item No. 1.1 in the left window.

Fill following values in the right window:

ELFORM: 2

SHRF: 1.0

NIP: 2

PROPT 0

QR/IRID: 0

ICOMP: 0

SETYP: 1

Select the item No. 2.1 in the left window.

Fill following values in the right window:

T1~T4 : 1.0

Property->ASSIGN

P-1->2 Tube->Apply

Property->ASSIGN

P-2->1 Die; 3 Punch; 4 Punch2->Apply

Contact

Contact->Create->3 Dimensions->*Contact_Automatic_Surface_To_Surface-> Next

Select the item No. 2.1 in the left window.

Fill following values in the right window:

SSID: 2

MSID: 1

SSTYP: 3

MSTYP: 3

Select the item No. 3.1 in the left window.

Fill following values in the right window:

FS: 5.0e-02

FD: 5.0e-02

Contact->Create->3 Dimensions->*Contact_Automatic_Surface_To_Surface-> Next

Select the item No. 2.1 in the left window.

Fill following values in the right window:

SSID: 2

MSID: 3

SSTYP: 3

MSTYP: 3

Contact->Create->3 Dimensions->*Contact_Automatic_Surface_To_Surface-> Next

Select the item No. 2.1 in the left window.

Fill following values in the right window:

SSID: 2

MSID: 4

SSTYP: 3

MSTYP: 3

Load Curves Defining:

DynaMisc->Load Curves->Create->inner_pressure->OK

Insert->Key-in->0,0

Insert->Key-in->18->31.5

OK

DynaMisc->Load Curves->Create->displacement->OK

Insert->Key-in->0,0

Insert->Key-in->18->65

OK

Boundary Conditions

BC->Boundary->Prescribed Motion

Select a node belongs to part Punch 2

DOF: 1

VAD: 2

LCID: 2

SF: -1.0

OK

BC->Boundary->Prescribed Motion

Select a node belongs to part Punch

DOF: 1

VAD: 2

LCID: 2

SF: 1.0

OK

BC->Load ->Segment Pressure->Create->Segement Set...->By Elements

Select all elements of the tube part.

LCID: 1

SF: -1

AT: 0

Create 4 Node Sets

Set->Node->Create

Select all nodes belongs to die part, named die

Select all nodes belongs to punch part, named punch

Select all nodes belongs to punch2 part, named punch2

Select all nodes belongs to the tube's inter-section lines, named tube_edge

BC->Boundary->SPC

Create->die

Select the item No. 2.1 in the left window.

Fill following values in the right window:

DOFX: 1

DOFY: 1

DOFZ: 1

DOFRX: 1

DOFRY: 1

DOFRZ: 1

OK

BC->Boundary->SPC

Create->Punch

Select the item No. 2.1 in the left window.

Fill following values in the right window:

DOFX: 0

DOFY: 1

DOFZ: 1

DOFRX: 0

DOFRY: 0

DOFRZ: 0

OK

BC->Boundary->SPC

Create->Punch2

Select the item No. 2.1 in the left window.

Fill following values in the right window:

DOFX: 0

DOFY: 1

DOFZ: 1

DOFRX: 0

DOFRY: 0

DOFRZ: 0

OK

BC->Boundary->SPC

Create->tube_edge

Select the item No. 2.1 in the left window.

Fill following values in the right window:

DOFX: 0

DOFY: 0

DOFZ: 1

DOFRX: 0

DOFRY: 0

DOFRZ: 0

OK

Now the model is built and ready to be solved.

II Solving

To solve a model from FEMB, it has to be converted as a dyn file.

In FEMB:

File->export->LS-DYNA(*.dyn)

Open LS-DYNA 970.

Solvers->start analysis->Input File->Browse

Select the .dyn file we have just exported

Click the "solve" button to solve the model.

III Post-Processing

Run program Post-Processor (POST GL 1.0)

File->open

Open the d3plot file which is generated by LS-DYNA.

We can observe different data by changing the list bar on the right panel.

Take von Mises stress distribution for example.

Select "Single Frame" in the Frames Pane.

Select the last time step.

Click "Contour" button on the top of the main window.

Select "MAX_VONMISES" in the menu named "Current Component".

A contour will be shown in the display window.

To observe the stress for a certain element, click "List Value" Button in the right window.

Use "Select by Cursor" option to pick a element that is to be observed.

The stress value will be listed in a table on the bottom of the display window.

Appendix B: Computer Programs

Program 1: cal_principal_stress.m

```
%This program deals with the principal stress calculation
%Output variables are principal stresses to be evaluated
%Input parameters are the stress components that are read from LS-DYNA
%output file, where, sigxx is the normal stress component along x axis,
%sigyy is along y axis, sig zz is along z axis, sigxy, sigxz, and sigyz are
%corresponding shear stresses.
%The corresponding equations can be found in section 1.4.
function [sig1,sig2,sig3] = cal_principal_stress(sigxx,sigyy,sigzz,sigxy,sigxz,sigyz)
%I1, I2 and I3 are the first, second and third stress invariants
%respectively
I1 = sigxx+sigyy+sigzz;
I2 = sigxx*sigyy+sigyy*sigzz+sigxx*sigzz-sigxy^2-sigyz^2-sigxz^2;
I3 = sigxx*sigyy*sigzz+2*sigxy*sigyz*sigxz-sigxy^2*sigzz-sigyz^2*sigxx-sigxz^2*sigyy;
%construct the polynomial equation for principal stresses.
p = [1 -I1 I2 -I3];
%solve the polynomial equation p.
r = roots(p);
%assign principal stress to sig1, sig2 and sig3
%Generally, sigma1 should be greater than sigma2, and sigma2 should be
%greater than sigma3. But those principal stresses are used for von mises
%stress caculation, this order doesn't needed.
sig1 = r(1);
sig2 = r(2);
sig3 = r(3);
```

Program 2: cal_von_mises_stress.m

```
%This program deals with the von Mises stress calculation
%The corresponding equation can be found in section 1.4.
function sigv = cal_von_mises_stress (sig1,sig2,sig3)
sigv = sqrt(0.5*((sig1-sig2)^2+(sig1-sig3)^2+(sig2-sig3)^2));
```

Program 3: cal_ductile_int.m

```
%This program deals with the ductile fracture integration that defined in
%section 1.4. The input parameter "steps" is the total time steps evaluated
%by LS-DYNA, this value is not the total time steps in the solving process,
%but the divided time ranges in the output file (d3plot) from LS-DYNA. In
%this program, steps is set to 22. The corresponding equations in this
%program can be found in section 1.4.
function cal_ductile_int(steps)
%C1 and C2 are material constants for AA5052-O.
C1 = 0.28; C2 = 0.3;
%Open a output file (*.lst) from LSDYNA and obtain a file id. A sample of
%a.lst file can be found in Appendix C.
fid=fopen('D:\FEA\Y Hydro\Dyn Files\model_V_5052\Curves.lst');
%skip the unuseful data in the list file.
for i = 1:3
    fgets(fid);
end
%Read data from file until the file ends
%The following while loop is used to read all stress components that are
%needed in program cal_pincripal_stress.m, which are sigxx, sigyy, sigzz,
%sigxz, sigxy, sigxz. The plastic strain is also recorded by this program
%for the ductile fracture integration. Matrix time is the time domain read
```

```
%from the list file (*.lst file). The index i means the current time step,
%e.g. sigxx(1) is the current normal stress along axis x at time step 1
%(which is time(1)). etc.
while(~feof(fid))
    fgets(fid);
    %record normal stress sigmax
    for i = 1:steps
        s = strread(fgets(fid));time(i) = s(1);sigxx(i) = s(2);
    end
    fgets(fid);
    %record normal stress sigmay
    for i = 1:steps
        s = strread(fgets(fid));
        sigyy(i) = s(2);
    end
    fgets(fid);
    %record normal stress sigmaz
    for i = 1:steps
        s = strread(fgets(fid));
        sigzz(i) = s(2);
    end
    fgets(fid);
    %record shear stress sigmaxy
    for i = 1:steps
        s = strread(fgets(fid));
        sigxy(i) = s(2);
    end
    fgets(fid);
    %record shear stress sigmayz
    for i = 1:steps
```

```
        s = strread(fgets(fid));
        sigyz(i) = s(2);
    end
    fgets(fid);
    %record shear stress sigmaxz
    for i = 1:steps
        s = strread(fgets(fid));
        sigzx(i) = s(2);
    end
    fgets(fid);
    %record plastic strain
    for i = 1:steps
        s = strread(fgets(fid));
        strain(i) = s(2);
    end
    fgets(fid);
end
%The following loop is used to evaluate the principal stress, von Mises stress
%and mean stress for every time step. function cal_principal_stress and fucntion
%cal_von_misses_stress is called here.
for i = 1:steps
    [sig1(i),sig2(i),sig3(i)] = cal_principal_stress(sigxx(i),sigyy(i),sigzz(i),sigxy(i),sigyz(i),sigzx(i));
    %von Mises stresses
    sigv(i) = cal_von_mises_stress(sig1(i),sig2(i),sig3(i));
    %mean stresses
    sigm(i) = (1/3)*(sig1(i)+sig2(i)+sig3(i));
    %mean stress over von Mises stress
%The following program deals with the ductile fracture integration. Three
%points numerical integration method is employed. The ductile fracture
%integration can be found in section 1.4.
```

```
    if sigv(i) == 0
        ratio(i) =0;
    else
        ratio(i) = sigm(i)/sigv(i);
    end
    sub_value(i) = ratio(i) + C2;
    if i > 1
        value_at_mid_point(i-1) = 0.5*(sub_value(i)+sub_value(i-1));
        delta_strain(i-1) = strain(i) - strain(i-1);
        int_value(i-1) = value_at_mid_point(i-1)*delta_strain(i-1)/C1;
    end
end
summ = 0;
%The following program evaluates the integration and draw a plot to show
%the changing trend for this integration w.r.t. time.
for i = 1:steps-1
    summ = summ+int_value(i);
    I_time(i) = summ;
    new_time(i) = 0.5*(time(i) +time(i+1));
end
plot(new_time, I_time)
xlabel('Time(ms)')
ylabel('Ductile Integration I')
I = sum(int_value)
end
```

Program 4: calForceWithTime.m

```
%This program deals with calculation of axial force needed in tube
%push-bending, the input parameter OD is the out diameter of the tube (in
%mm); Unlike cal_ductile_int.m, in this program, a .col output file from
```

```
%LS-DYNA's post-processor is used. Because many shell elements are involved in
%this programm, the use of a *.col file is more convenient. Data in the
%.col file can be imported to MATLAB as a big matrix. The construct of a
%.col file is given in Apendix D.
function calForceWithTime(OD)
%Read the output file and obatin a file id.
filename = 'D:\FEA\Push Bending\LS-DYNA Models\50.80OD_54DIE\50.8OD_2D\1.25mm\output.col';
fid=fopen(filename);
fgets(fid);
%Obtain the number of elements included in the output file;
nElementFromFile = strread(fgets(fid));
%Obtain the total time steps, see comments in cal_ductile_int.m
nSteps = strread(fgets(fid));
%calculate the element edge length along the circumferential direction
elementLength = 0.5*pi*OD/(nElementFromFile/2);
%read the whole output file as a big matrix A;
A = csvread(filename, nElementFromFile+3, 0)
%The following loop deals with the construction of the axial load vector.
%nForce is the axial load at current time step, because of the symmetry of
%the FEM model, the real axial load needed is double quantity of nForce.
%nFoce is evaluated by adding all sub_forces at every shell element. the
%force at a element can be obtained by multiplying the cross-sectional
%area and the normal stress along the axial direction. Then the axial load
%vector 'force' is constructed.
for i= 1:nSteps
    nForce = 0;
    for j = 2:2:nElementFromFile
        stress(i,j/2) = A(i,j);
        nStress = stress(i,j/2);
```

```
        nThickness = A(i,j+1);
        nForce = nForce + nStress*nThickness*elementLength;
    end
    force(i) = nForce*2;
end
%Obtain the time range from matrix A.
time = A(:,1);
%Plot the curve
plot(time,abs(force))
xlabel('time (s)')
ylabel('axial force (N)')
```

Program 5: calStressWithAngle.m

```
%This program deals with evaluation of the stress distribution at cross-section
%B (see Fig. 4.5) along the cirumferential direction in tube push-bending.
%The angle definition can be found in Fig. 4.9. The input parameter 'OD' is
%the out diameter of the tube (in mm); input parameter 'step' is the time
%step when the stress distribution is generated. Changing value of 'step',
%stress distribution can be observed at different time step.A '.col' output
%file from LS-DYNA's post-processor is used.  The construct of a .col file
%is given in Apendix D.
function calStressWithAngle(OD,step)
%Read the output file and obatin a file id.
filename = 'D:\FEA\Push Bending\LS-DYNA Models\50.80OD_54DIE\50.8OD_2D\1.25mm\oo.col';
fid=fopen(filename);
fgets(fid);
%Obtain the number of elements included in the output file;
nElementFromFile = strread(fgets(fid));
%Obtain the total time steps, see comments in cal_ductile_int.m
nSteps = strread(fgets(fid));
```

```
%read the whole output file as a big matrix A;
A = csvread(filename, nElementFromFile+3, 0);
%The following loop deals with the construction of the stress vector.
for i= 1:nSteps
    for j = 2:2:nElementFromFile
        stress(i,j/2) = A(i,j);
    end
end
%select a series of stresses at a certain time step.
stress1 = stress(step,:)
%obtain the increasement of angle.
dTheta = 180/(nElementFromFile/2);
theta = [dTheta:dTheta:180];
%plot the curve.
plot(theta,stress1)
xlabel('0 \leq \Theta \leq 180 (dgree)')
ylabel('normal stress (MPa)')
```